© 2011 Adam Matthew Willis

ENHANCED DROPLET SPREADING DUE TO THERMAL FLUCTUATIONS

BY

ADAM MATTHEW WILLIS

DISSERTATION

Submitted in partial fulfillment of the requirements
for the degree of Doctor of Philosophy in Theoretical and Applied Mechanics
in the Graduate College of the
University of Illinois at Urbana-Champaign, 2011

Urbana, Illinois

Doctoral Committee:

Professor Jonathan Freund, Chair
Professor Sasha Hilgenfeldt
Professor Richard Weaver
Assistant Professor David Saintillian

To my family, for the support they have given me throughout this whole process. To Col. Geoffrey Ling for his critical support and guidance through the process of becoming a medical researcher in the United States Air Force. To my advisor Jonathan B. Freund, for the tireless energy he applied in order to train me to think, analyze, and solve problems. All of my future work will undoubtedly bare the hallmarks of his effort.

Table of Contents

List of Tables

List of Figures

Chapter 1

Introduction

Thin liquid films ($<$ 100 nm thick) and their dynamics are important in applications such as MEMS, cooling devices, biomedical tools,[1,2] microelectronics,[3] and photonics.[4] Under ordinary conditions the motion of the fluid at such scales is, of course, Stokesian, governed by a balance between viscous stresses and pressure gradients, which are generated by external stresses or body forces. However, as films approach molecular scales, the motion of the fluid can also be affected by the fluctuations arising from the thermal energy of the fluid as well as the granular nature of its underlying molecular structure. The interplay between this stress and the Laplace pressure due to surface tension is manifested in dynamic perturbations of a liquid-vapor interface about its equilibrium profile.

There are several cases in which these thermal fluctuations have been shown to play a significant role in small-scale flow dynamics, and they therefore need to be included into models to accurately predict the overall flow behavior. For example, Moseler and Landman[5] demonstrated that a stochastic force must be included in the governing equations in order to qualitatively match the breakup dynamics of a simulated molecular nanometer-scale jet. The neck formed in the breakup of these jets display a power law that was shown by Eggers[6] to be characteristic of thermal fluctuations coupled to the hydrodynamics. There is also laboratory evidence for such a coupling. In a series of experiments using a colloid-polymer, Aarts *et al.*[7] suggested that thermal fluctuations play a key role in the coalescence of droplets. Similarly, Hennequin *et al.*[8] were able to demonstrate that the dynamics of droplet rupture, including the resulting droplet size distribution, is affected by the amplitude of thermal fluctuations on the interface. The necking dynamics of these ruptures also conform to the predictions of Eggers.[6]

There are also theoretical predictions of changes in thin film dynamics due to thermal fluctuations. Davidovitch *et al.* [9] suggest that thermal fluctuations can accelerate the spreading of a fluid drop on a surface and predict a $t^{\frac{1}{4}}$ spreading that is faster than the predicted Tanner's law spreading power law of $t^{\frac{1}{7}}$. Studying a similar system, Grun *et al.*[10] show that numerical solutions of a stochastic differential equation, which models thermal fluctuations as internally applied stresses, suggest a decrease in the rupture time of unstable thin liquid films by almost an order of magnitude.

1.1 Thermal Fluctuations from Molecular Granularity

Obviously, not all models of fluid film interfaces require considerations of thermal energy. Often, the only effect temperature has upon film behavior is contained within the temperature dependent continuum parameters, such as viscosity η and surface tension γ. By using dimensional analysis, one can estimate the length scale of thermal perturbations in a fluid interface, l_t, and thus at what length scales thermal fluctuations might affect mechanics:

$$l_t = \sqrt{\frac{k_B T}{\gamma}}, \tag{1.1}$$

where $k_B T$ is a measure of the thermal energy of the fluid. For many fluids, l_t is on the order of angstroms. For example, the thermal length of ethyl alcohol at 20 $^{\circ}C$ is 4.26 Å. This length scale is on the same order as the size of ethyl alcohol molecule, which has a radius of gyration of 2.259 Å.

As in ethyl alcohol, thermal fluctuations for many fluids will become non-negligible at length scales near the size of the molecules that make up the fluid. At sufficiently small scales, a continuum approximation necessarily fails. It simply cannot describe the motion of individual atoms. However, it is unclear at what length scale this failure occurs relative to the scale at which thermal fluctuations become important. While these are both expected to be atomic scales, it is known that the continuum model is remarkably effective to just a few atomic/ molecular lengths[11,12] The

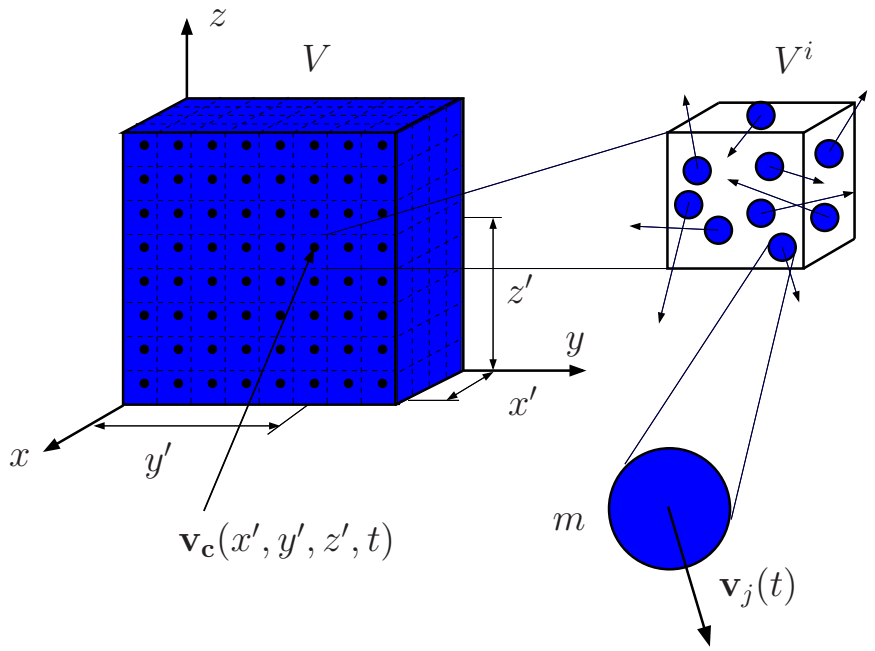

Figure 1.1: Continuum representation of fluid volume V that is composed of subdomains V^i, centered around the point (x', y', z'). The continuum velocity at that point is $\mathbf{v}_c(x', y', z', t)$. The total volume of fluid has N atoms where as each subdomain V^i has at any one moment N^i atoms contained within. Each atom j has mass m and velocity $\mathbf{v}_j(t)$.

possibility of augmenting it with stochastic stresses to model thermal fluctuations within a continuum description has been proposed.[5,9,10,13]

Assuming that a continuum model can contain the appropriate physics to model the behavior of thermally fluctuating fluid interfaces, we can directly test means of incorporating thermal fluctuations fit into a continuum description. But, how is it that thermal fluctuations cannot be averaged out in small length scale flows as they are in classical fluid analysis?

To answer this question, consider the model problem shown in Figure 1.1 of a volume of fluid V containing N fluid atoms held at a constant temperature T. For simplicity assume boundary conditions are periodic and the fluid atoms are all the same mass m. As shown in Figure 1.1, the domain is discretized into adjacent subdomains where the ith domain, V^i, contains N^i atoms and is centered around the point (x', y', z'). The continuum velocity of this point at time t is $\mathbf{v}_c(x', y', z', t)$. The assumption is that this continuum velocity is continuous and will obey the Navier-Stokes

equations if the definitions of pressure and the fluid's constitutive model are appropriately chosen. It is about the values of $\mathbf{v}_c(x', y', z', t)$, the thermal fluctuations of the velocity field are assumed to fluctuate.

Starting at some point arbitrarily defined as $t = 0$ the average velocity of subdomain i, centered at point (x', y', z') over time τ is $\mathbf{v}_a(x', y', z', \tau)$ where

$$\mathbf{v}_{\mathrm{a}}(x', y', z', \tau) = \int_0^\tau \frac{1}{N^i \tau} \sum_{i=1}^{N^i} \mathbf{v}_i(t) \mathrm{d}t, \tag{1.2}$$

and could be measured if one had access to the atomic velocities as a function of time. Also note, that the continuum velocity is not a quantity that can be measured directly, but as will be shown, assuming a certain form of thermal fluctuations, the continuum velocity is what is left after an ensemble average of atomic motion. More exactly, there is an assumption made that there does exist a continuum value of velocity, about which the thermal velocities fluctuate. Thus each atom j in subdomain i has a velocity that is a combination of the continuum flow of that subdomain $\mathbf{v}_c$ and a random thermal velocity $\mathcal{V}_j$ such that,

$$\mathbf{v}_{\mathrm{a}}(x', y', z', \tau) = \frac{1}{N^i \tau} \int_0^\tau \sum_{j=1}^{N^i} \left(\mathbf{v}_c(x', y', z', t) + \mathcal{V}_j(t) \right) \mathrm{d}t. \tag{1.3}$$

A further assumption is that the continuum velocity does not change appreciably over the time scales over which the velocity is averaged. Thus it can be considered constant throughout the averaging, leading to

$$\mathbf{v}_{\mathrm{a}}(x', y', z', \tau) = \mathbf{v}_c(x', y', z', \tau) + \frac{1}{N^i \tau} \sum_{j=1}^{N^i} \int_0^\tau \mathcal{V}_j(t) \mathrm{d}t. \tag{1.4}$$

This the continuum velocity $\mathbf{v}_c$ will be different from the measured, averaged velocity $\mathbf{v}_a$ by $|\frac{1}{N^i \tau} \sum_{j=1}^{N^i} \int_0^\tau \mathcal{V}_j(t) \mathrm{d}t|$. This fluctuation term is the sum of the integrations over the averaging time τ of all the molecules within the subdomain i. An assumption used to simplify this term and simplify the description is that the random motions of each molecule are independent of each other. This is not an unreasonable assumption for length and time scales much greater than molecular correlation times and lengths. For many engineering problems length and times scales are orders of magni-

tudes greater than molecular scales. Rahman[14] showed via a model of liquid argon that the atomic velocity of a fluid decorrelates on the order of 10 picoseconds and density decorrelates on a length scale of the atomic radii (3.405 angstroms for argon). Thus it is assumed that there are enough collisions during the integration period of τ that the central limit theorem can be employed and the velocity fluctuations approach the behavior of a zero mean, Gaussian random variable.

With this assumption of a Gaussian random process, our goal is to quantify the variance of this difference between averaged velocity $\mathbf{v}_a$ and the bulk flow or continuum velocity $\mathbf{v}_c$. The amplitude of the variance for this Gaussian random variable can then be quantified by realizing that the integration in time of $\mathcal{V}_i$ is a random walk $\mathbf{r}(t)$. For fluids, the magnitude of the correlations of this random walk corresponds to the macroscopic coefficient known as the diffusion coefficient, D, such that

$$E\left[\mathbf{r}(t)^2\right] = E\left[\left(\int_0^\tau \mathcal{V}_i \mathrm{d}t\right)^2\right] = 6D\tau, \tag{1.5}$$

where $E[...]$ is the expectation value or ensemble average defined in Section 2.1.1. For reference, the diffusion coefficient of water at 25 $^\circ C$ is $2.272 \times 10^{-6} m^2/s$.

This random walk can be modeled using a Brownian motion, which is a continuous stochastic process used to model diffusions.[15] This model will be further explained in Section 2.1.1. The magnitude of the diffusion distance, or root-mean-squared displacement, $|\mathbf{r}(t)|$, can be transformed into a normalized Brownian motion, B_t such that

$$|\mathbf{r}(t)| = \sqrt{6D}B_t. \tag{1.6}$$

In (1.4) the magnitude of the difference between the continuum velocity and the averaged velocity, R_τ, can be quantified as

$$R_\tau = |\mathbf{v}_\mathrm{a}(x', y', z', \tau) - \mathbf{v}_c(x', y', z', \tau)| = \frac{1}{N^i \tau} \sum_{j=1}^{N^i} \sqrt{6D} B_\tau^j, \tag{1.7}$$

where B_τ^j is the position of the Brownian motion of particle j in one di-

mension at time τ, where $B_0^j = 0$. This is consistent with our model because the Brownian motion is the model of how far each particle traveled in time t, thus at time $t = 0$ this distance is obviously zero. The average of a diffusion (i.e. Brownian motion) is zero. Because of the relatively short decorrelation lengths of the velocity and the short decorrelations times, for averages over volumes and times much greater than molecular length scales and vibrational time scales, it is not unreasonable to approximate that each particle behaves independently and thus is an independent Brownian motion. With this assumption, the variance of R_t becomes

$$E[R_t^2] = E\left[\left(\frac{\sqrt{6D}}{N^i\tau}\sum_{j=1}^{N^i} B_t^j\right)^2\right] = \frac{6DN^i\tau}{(N^i)^2\tau^2} = \frac{6D}{N^i\tau}. \tag{1.8}$$

Thus, by this analysis, thermal fluctuations average out of the averaged fluid flow and decrease as a function of $\frac{1}{\sqrt{N^i\tau}}$. The assumption used here to separate out thermal fluctuations into decorrelated, Gaussian white noise, is the same set of assumptions that are used to include thermal fluctuations into the continuum equations, as will be discussed in Section 2.3 and used in models by others[5,9] for thermally perturbed fluid equations.

Essentially, in these models the effect of thermal fluctuations is bundled into an uncorrelated Gaussian white noise term. Other continuum variables could similarly be analyzed in terms of thermal fluctuations.[13,16] Although different continuum variables would have different magnitudes of fluctuations, the thermal fluctuations in averaged quantities would still scale as $\frac{1}{\sqrt{N^i\tau}}$. Thus for large numbers of particles, or for longer periods of time averageing of particles, thermal fluctuations will not modify the averaged values significantly and the averaged values converge to the continuum values for which continuum analysis applies. Conversely for short integration times and for control volumes with few particles, the thermal fluctuations may perturb averaged values of variables significantly.

1.2 Present Objectives

Our particular objective here is to assess directly whether or not there exists a length scale which adding a model of uncorrelated thermal noise to a continuum model is inadequate, either because the thermal motion of atoms contains some non-negligible correlations or that averaged fluid behavior exhibits some characteristics due to the spatial extent of the fluid molecule.

More precisely, there must exist some length scale where the fluid behavior, even after accounting for thermal fluctuations with an idealized noise term, will be affected by the size of its constitutive particles. The first question of this dissertation is whether this length scale of expected continuum break down is near the length scale at which thermal fluctuations affect mechanics. A model problem in which to investigate this question is studying the dynamics of thermal capillary waves, which are the small amplitude perturbations in a fluid interface due to thermal fluctuations.

1.2.1 Thermal Capillary Waves

Previously there have been many efforts to assess the applicability of continuum predictions of the amplitude and decay rate of thermal capillary waves on thin stable liquid films.[17–24] The dynamics of these waves, as compared to the dynamics in droplet rupture[10] or spreading,[9] have simple hydrodynamic solutions, which facilitate direct comparisons to continuum models.

Thermal capillary waves are challenging to study experimentally, especially in simple fluids, because of their extremely fast time scales ($\sim 10^{-11}$ s) and short length scales ($\sim 10^{-10}$ m). X-ray spectroscopy is being used in current experimental efforts[17–19,21,24] to resolve the small length scales while complex fluids, such as colloid-polymer systems and thin polystyrene films, are being used to slow down the time scales and increase the length scales of the thermal waves. Colloid-polymer systems can have surface tensions 10^6 times smaller than simple fluids,[7,8] which increases the amplitude

of the capillary waves. These conditions make colloid-polymers useful for phenomenological studies,[7] but it also introduces a fundamental limitation when comparing with theory. Because the film thickness cannot be precisely controlled and fluid properties are complex and undocumented, direct comparisons to continuum models is impossible. Polystyrene films also suffer similar limitations. Although polystyrene is attractive because of its slow time scales, and unlike colloid-polymers particular thicknesses are easy to manufacture, these films exhibit complex behavior near solid-liquid and liquid-vapor interfaces. The visco-elastic properties of these fluids affect amplitude statistics,[17,18] in cases yielding multiple exponential decay rates for individual wave numbers.[22] The dynamics may also be altered by absorption of polymer chains onto the solid substrate[24] or changes in the effective viscosity near the surface,[17,25] which also makes it difficult to separate complex material behavior from the general behavior of capillary waves on thin films.

There has been some success in comparing particularly short-chain polystyrene films to Newtonian fluids in thin films.[26] However, the radius of gyration of even these shorter molecules is still an appreciable fraction of the film thickness, which has been shown to have non-Newtonian features.[17,18,24,25] This apparent contradictory evidence highlights the challenge of making conclusive inferences on thin-film behavior from polystyrene films alone.

For our assessment, we use idealized but realistic atomistic simulations to provide simple-fluid data for directly assessing the breakdown of the continuum description for the decay of thermal capillary waves. This first project focused upon the dynamics of thermal capillary waves, the small perturbations of a stable, constant thickness, liquid-vapor interface due to thermal fluctuations. These small perturbations in the fluid-vapor interface allow the linearization of the Navier-Stokes equations and thus an analytic solution to the decay rates of thermal capillary waves as a function of the wavenumber as described by Henle *et al.* [22] By comparing the predictions of the continuum equations with the dynamics of a molecular fluid interface for several different lengths of molecular polymers, we demonstrated the validity of both the Newtonian viscous fluid model and the Laplace surface pressure model for perturbation wavelengths as small as

20 molecular radii of gyrations of the constitutive fluid molecules. However, our analysis also found an unexpected deviation in the decay rates of the perturbations for perturbation lengths of less than 20 molecular radii of gyration. As will be shown in Chapter 4, this deviation suggests the effective dissipation of the molecular fluid in this new regime is still proportional to the Newtonian viscosity (a continuum concept) but is also influenced by the fluid's molecular size (a granular concept).

The accurate modeling of the the averaged dynamics of capillary waves down to length scales on the order of 20 molecular radii is encouraging for further probing of thermally driven fluid film behavior with continuum models. However, thermal capillary waves are small enough to be linearized and were studied in an equilibrium film, which is not generalizable to other thin film problems[27] where the films are often not in equilibrium and dynamics are not linear. It is unclear if the success of the linearized continuum equations will be carried over to make predictions in the larger regime of nonlinear, non-equilibrium thin film behavior that is driven by thermal fluctuations. Also, despite there being theoretical predictions that thermal fluctuations can affect film dynamics as perturbations to an interface,[5,10] there has been no direct evidence that thermal fluctuations can drive bulk flow or that thermally augmented equations could quantitatively predict thermally driven flow.

1.2.2 A Spreading Drop on a Solid Wall

An effort to demonstrate the necessity of including thermal fluctuations into certain fluid models along with a desire to further demonstrate the accuracy of continuum modeling to predict the behavior of thermally driven thin film flow, led to the second project of this dissertation.

Davidovitch *et al.*[9] suggests that thermal fluctuations could dominate the spreading of a fluid droplet on a wetting plate, leading to droplet spreading that would increase the width of a self-similar drop as a power-law in time of $t^{1/4}$ (as opposed to classic surface tension spreading which scales like $t^{1/7}$). In this second project, we test predictions of thermally augmented continuum equations against the spreading of a simulated molecular drop. Unlike the first project, the interface dynamics of a thermally

driven spreading drop are not small perturbations of an equilibrium profile. Rather, this second project studied the spreading of a non-equilibrium fluid drop upon a wetting plate under conditions predicted to show thermally dominated spreading dynamics.

Efforts to model the dynamics of thin liquid films, where thermal fluctuations may drive nonlinear dynamics, often rely upon a simplifications of the full Navier–Stokes equations. This simplification is usually founded on an assumption of a small capillary number $Ca \equiv \eta U/\gamma$, where U relevant is a velocity scale. For our discussions η and γ are assumed constant. When the thickness of the film d is much smaller than its other spatial dimensions, say λ, a long-wave approximation $\lambda \gg d$ is also employed giving the so-called lubrication limit of the flow equations. With these assumptions and standard no-slip and stress-balance boundary conditions at the wall and free surface, a single partial differential equation can be constructed that governs the film thickness $h(x,t)$.[28] Further modifications may be included to account for the evaporation dynamics of non-equilibrium films.[29]

Previously, atomistic simulations of model fluids have been used effectively to investigate the role of stochastic thermal stresses,[5] and we take this approach to assess the stochastic lubrication equation for drop spreading. For this second project of this dissertation, we accept that the model provided by empirical atomic interaction potentials is sufficiently realistic to test the assertions in the stochastic lubrication equations, then the primary limitation of the scope of such an investigation is its computational cost. The key distinction between this work and previous atomistic simulations of spreading drops[30,31] is that our simulation is specifically designed to examine the thermally dominated regime by using a large, three-dimensional, relatively long-time simulation of a simple-fluid, low-viscosity drop. Further realism needed to be included in this project to account for the long-time evaporation of our non-equilibrium fluid film. To do so, we use the framework of Ajaev *et. al*[29] which has been used to successfully predict the evaporative mass flux through an atomic scale meniscus.[11]

1.3 Organization of this Dissertation

Starting from essentially first principles, Chapter 2 discusses the underlying theory of the incorporation of thermally perturbed thin liquid films into continuum models, and how they can be then used to predict the behavior of perturbations in thin liquid films due to thermal fluctuations. Chapter 3 discusses the numerical techniques used to model thin liquid films, including molecular simulations algorithms and the algorithms used to solve stochastic partial differential equations. Chapter 4 is a study which analyzes the linearized behavior of flat, stable, thin liquid films in order to assess the validity of different components of the continuum model for a range of length scales. Chapter 5 is a comparison between molecular simulations of a spreading drop and the stochastically augmented lubrication equation which is designed to model such spreading behavior. Conclusions are summarized in Chapter 6.

Chapter 2

Theory Framework

This dissertation is composed of two main projects. The first project (Chapter 4) is the study of the time correlations of thermal capillary waves in stable fluid films. Thermal capillary waves are small perturbations in an equilibrium interface due to thermal fluctuations. The small amplitudes of the thermal capillary waves permits the linearization of the Stokes equations, yielding closed solutions to the time correlation decay rates as a function of the wavenumber of the perturbation. Using the explicit solution of the continuum predictions and directly comparing them with the measured behavior of simulated molecular fluids we will be able to assess at what length scales the continuum model fails. In Section 2.2 of this chapter, the model problem of thermal capillary waves will be defined along with the closed solution for the correlation decay rate as a function of wavenumber.

The second project of this dissertation studies the spreading of a molecular drop on a wetting solid surface in a regime where thermal fluctuations are predicted to dominate capillary forces and accelerate spreading. In Section 2.4 of this chapter the model problem of droplet spreading will be defined. Additionally, following the work of Davidovitch *et al.*,[9] we develop the analysis that predicts the enhanced spreading rate due to thermal fluctuations. Then, in Section 2.3, following the analysis of Grun,[10] a thermally augmented continuum model of the interface dynamics in a thin liquid film is developed. This so-called stochastic lubrication equation model will be used for direct comparison to a spreading molecular drop. We include an evaporation model (in Section 2.3.1) in these continuum equations to account for the evaporation of the spreading drop seen in the atomistic simulations.

However, before discussing the theoretical preliminaries particular

to each project of this dissertation, the generalized mathematical concepts used to represent thermal fluctuations within continuum models, namely, stochastic differential equations are introduced. The models of thermal noise used in the modeling of thermally perturbed continuum equations are built upon a Gaussian white–noise term, which when integrated produces Brownian motion.[15] Brownian motion is introduced as the foundation of stochastic differential equations in Section 2.1.1. The integration used in the solution of stochastic differential equations (introduced in Section 2.1.2), namely Ito integration, will be discussed in Section 2.1.3. Using Ito integration, the solution of a first–order stochastic differential equation will be demonstrated in Section 2.1.4. In Chapter 4, the solution of this general first–order stochastic differential equation will be used to obtain the continuum predictions of the time correlations of thermal capillary waves. Discussed in Section 2.1.5 is the method for determining the size of thermal fluctuations that satisfy equilibrium statistics when dissipation is modeled via the Newtonian stress tensor. This amplitude is necessary in the development of a stochastically driven lubrication equation, which will be used in the second project of the dissertation (Chapter 5).

2.1 Stochastic Differential Equations

The integration of stochastic differential equations requires a careful examination of the definition of integration which leads to subtle differences from traditional Riemann calculus. The stochastic forcing included in physical models of thermal fluctuations is defined as the time derivative of a mathematical model of Brownian motion B_t. A more complete development of stochastic differential equations can be found in Oksendal.[15]

2.1.1 Brownian Motion

Brownian motion was originally attributed to the seemingly stochastic motion of a pollen particle suspended within a fluid. This motion was first characterized by Robert Brown in 1828 and physically is due to the impacts of surrounding fluid molecules against the pollen grain. In this disser-

tation we will refer to the mathematical abstraction of this process $B_t(\omega)$. Assuming that particles are confined to move in a single spatial dimension, the random variable $B_t(\omega)$ represents the position of a Brownian particle ω at time t. For convenience, the initial position ($t = 0$) of particle ω is zero: $B_0(\omega) = 0$. Assuming that all possible pollen particles are contained in the set Ω, such that $\omega \in \Omega$, the expectation value operator of any random variable $X(\omega)$ is defined as

$$E[X] = \int_\Omega X(\omega) \mathrm{d}P(\omega), \tag{2.1}$$

where $\mathrm{d}P(\omega)$ is the probability density of particle ω. In one dimension the probability of $B_t(\omega)$, the position of particle ω at time t, being at a location greater than x, follows the behavior of a normalized, Gaussian random variable,

$$P[B_t(\omega) \leq x] = \int_{-\infty}^{x} \frac{1}{2\pi t} \exp\left(-\frac{x^2}{2t}\right) \mathrm{d}x. \tag{2.2}$$

This implies both

$$E[B_t(\omega)] = 0 \qquad \text{and} \qquad E\left[(B_t(\omega) - B_s(\omega))^2\right] = t - s \quad \text{if} \quad t \geq s. \tag{2.3}$$

$B_t(\omega)$ is also designated to have independent increments, which means that if a time interval $[0, T]$ is broken up into k discrete points, with $t_j > t_i$ when $j > i$, then the change in position of a particle during a time interval $[t_i, t_j]$ is independent of change during another time interval. These change in positions, $B_{t_1}(\omega), B_{t_2}(\omega) - B_{t_1}(\omega), ..., B_{t_{k+1}}(\omega) - B_{t_k}(\omega)$, are themselves random variables and the independence of each implies

$$E[(B_{t_k} - B_{t_{k-1}})(B_{t_j} - B_{t_{j-1}})] = 0, \qquad j \neq k. \tag{2.4}$$

Brownian motion will be used to develop the integration of stochastic differential equations. For the remainder of this work, unless otherwise specified, all random variables will be functions of ω, with ω being generalized to be one instance among the set of all possibilities Ω, and a stochastic process $X_t(\omega)$ will be represented by X_t.

2.1.2 Definition of Stochastic Integration

A general first-order stochastic differential equation of a random variable X_t has the form

$$\frac{\mathrm{d}X_t}{\mathrm{d}t} = b(t, X_t) + \sigma(t, X_t)W_t, \tag{2.5}$$

where W_t is a white–noise term, and $b(t, X_t)$ and $\sigma(t, X_t)$ are continuous functions of both time t and the random variable X_t. X_t could represent some physical process with a linear growth rate of $b(t, X_t)$ that is also driven by some random forcing W_t, with amplitude $\sigma(t, X_t)$. However, because of the large body of analysis and rigorous theoretical framework based upon Brownian motion,[15] it is convenient to cast the stochastic white-noise term W_t as a generalized white noise process $\mathrm{d}B_t/\mathrm{d}t$, which is derived from a Brownian motion, B_t.[15] Thus, (2.5) is re-cast as

$$\mathrm{d}X_t = b(t, X_t)\mathrm{d}t + \sigma(t, X_t)\mathrm{d}B_t, \tag{2.6}$$

which when integrated in time from $t = 0$ to $t = T$, yields

$$X_T = X_o + \underbrace{\int_0^T b(s, X_s)\mathrm{d}s}_{\text{Deterministic}} + \underbrace{\int_0^T \sigma(s, X_s)\mathrm{d}B_s}_{\text{Stochastic}}, \tag{2.7}$$

where X_o is the $t = 0$ value of X_t. The definition of the integral in (2.7) is defined as

$$X_T = X_o + \lim_{m\to\infty}\left[\underbrace{\sum_{j=0}^{m-1} b(t_{j^*}, X_{t_{j^*}})\Delta t}_{\text{Deterministic}} + \underbrace{\sum_{j=0}^{m-1} \sigma(t_{j^*}, X_{t_{j^*}})\Delta B_j}_{\text{Stochastic}}\right] \tag{2.8}$$

such that $\Delta B_k \equiv B_{t_{k+1}} - B_{t_k}$ and $\Delta t = T/m$. For each element j of the summation, a point t_{j^*} within the interval of $[t_j, t_{j+1}]$ is chosen at which to evaluate $\sigma(t_{j*}, X_{t_{j^*}})$, and $b(t_{j^*}, X_{t_{j^*}})$. When evaluating the deterministic summation of (2.8), the value t_{j^*} within the interval does not effect the result in the $\Delta t \to 0$ limit, however it does affect the result of the stochastic portion of the sum, as shown by Oksendal.[15] In order to define the stochastic integral, we choose $t_{j^*} = t_j$. This choice leads to a stochastic calculus

known as Ito calculus.[15]

2.1.3 Ito Calculus

Ito calculus has the following differentiation rule, upon which the Ito integral is based. Assuming a stochastic processes X_t can be constructed via (2.7) and a function $g(t, x)$ that is differentiable in time and twice differentiable in x, the differential of a stochastic process $Y_t = g(t, X_T)$ is

$$\mathrm{d}Y_t = \frac{\partial g(t, X_t)}{\partial t}\mathrm{d}t + \frac{\partial g(t, X_t)}{\partial x}\mathrm{d}X_t + \frac{1}{2}\frac{\partial^2 g(t, X_t)}{\partial x^2} \cdot (\mathrm{d}X_t)^2, \tag{2.9}$$

and $\mathrm{d}X_t^2 = \mathrm{d}X_t \cdot \mathrm{d}X_t$ is computed via

$$\mathrm{d}t \cdot \mathrm{d}t = \mathrm{d}B_t \cdot \mathrm{d}t = \mathrm{d}t \cdot \mathrm{d}B_t = 0 \qquad \text{and} \quad \mathrm{d}B_t \cdot \mathrm{d}B_t = \mathrm{d}t. \tag{2.10}$$

The choice of Ito calculus implies that the integral "$\int_0^t \sigma(s, X_s)\mathrm{d}B_s$" has several properties, namely if $f(t, \omega)$ and $g(t, \omega)$ are stochastic processes, and $0 < S < U < T$,[15]

$$\int_S^T f\mathrm{d}B_t = \int_S^U f\mathrm{d}B_t + \int_U^T f\mathrm{d}B_t, \tag{2.11}$$

$$\int_S^T (cf + g)\mathrm{d}B_t = c \cdot \int_S^T f\mathrm{d}B_t + \int_S^T g\mathrm{d}B_t \quad (c \text{ is constant}), \tag{2.12}$$

$$E[\int_S^T f\mathrm{d}B_t] = 0, \quad \text{and} \tag{2.13}$$

$$E\left[\left(\int_S^T g\mathrm{d}B_t\right)^2\right] = E\left[\int_S^T g^2\mathrm{d}t\right]. \tag{2.14}$$

Equation (2.14) is also known as Ito isometry and will be used in the analysis of the Orenstein-Uhlenbeck process.

2.1.4 Solution to Orenstein-Uhlenbeck Process

A basic stochastic differential equation is the Orenstein-Uhlenbeck (O-U) process, which has a differential form

$$\mathrm{d}X_t = bX_t\mathrm{d}t + \sigma\mathrm{d}B_t, \tag{2.15}$$

where $b < 0$ is the linear dissipation coefficient and σ the amplitude of the random forcing. This process often models physical systems with linear dissipation and stochastic perturbation such as the velocity of a Brownian particle suspended in a viscous fluid and Johnson noise in electrical circuits.[16]

One can easily solve for the behavior of X_t in (2.15) by using an integrating factor and the Ito equation (2.9). Letting $Y_t = e^{-bt}X_t$,

$$\begin{aligned} \mathrm{d}Y_t &= -be^{-bt}X_t + e^{-bt}\mathrm{d}X_t + 0 \\ &= -be^{-bt}X_t + e^{-bt}\left(bX_t\mathrm{d}t + \sigma\mathrm{d}B_t\right) \\ &= e^{-bt}\sigma\mathrm{d}B_t. \end{aligned}$$

Integrating $\mathrm{d}Y_t$ yields

$$\begin{aligned} Y_t &= Y_o + \int_0^t \sigma e^{-bt}\mathrm{d}B_t \\ e^{-bt}X_t &= Y_o + \int_0^t \sigma e^{-bt}\mathrm{d}B_t \\ X_t &= X_o + e^{bt}\int_0^t \sigma e^{-bt}\mathrm{d}B_t. \end{aligned}$$

This solution can be used to calculate the mean-squared expectation of X_t, by assuming that the initial position of X_o is at the origin and then employing Ito isometry (2.14),

$$\begin{aligned} E[X_t^2] &= E[X_o^2] + E[2X_o e^{bt}\int_0^t e^{-bs}\mathrm{d}B_s] + E\left[e^{2bt}\sigma^2\left(\int_0^t e^{-bs}\mathrm{d}B_s\right)^2\right] \\ &= 0 + 0 + e^{2bt}\sigma^2\int_0^t e^{-2bs}\mathrm{d}s \\ &= \frac{\sigma^2 e^{bt}}{2b} - \frac{\sigma^2}{2b}. \end{aligned}$$

The long-time or "stationary" average of an O-U process is equivalent to the ensemble average over all possible paths $\langle X_t\rangle$, thus assuming $b < 0$,

$$\langle X_t^2\rangle = -\frac{\sigma^2}{2b}. \tag{2.16}$$

This result will be used in the establishment of the fluctuation-dissipation theorem in Section 2.1.5.

The solution to the mean squared amplitude of an O-U process (2.16) can then be used to establish the behavior of the time correlations of an O-U process. Starting with the stochastic differential equation of an O-U process (2.15), multiplying by the initial value X_o, and taking the ensemble average

$$\begin{aligned} \mathrm{d}X_t &= bX_t\mathrm{d}t + \sigma\mathrm{d}B_t \\ \mathrm{d}\langle X_oX_t\rangle &= b\langle X_oX_t\rangle\mathrm{d}t + \sigma\langle X_o\mathrm{d}B_t\rangle. \end{aligned}$$

The ensemble average of a non-stochastic term multiplied by a white noise term $\mathrm{d}B_t$ is zero, thus

$$\mathrm{d}\langle X_oX_t\rangle = b\langle X_oX_t\rangle\mathrm{d}t, \tag{2.17}$$

which is a simple ODE with the solution,

$$\langle X_oX_t\rangle = \langle X_o^2\rangle e^{bt}. \tag{2.18}$$

When $b < 0$ the value of $\langle X_o^2\rangle$ is (2.16), thus the correlation behavior of an O-U process becomes

$$\langle X_oX_t\rangle = -\frac{\sigma^2}{2b}e^{bt}. \tag{2.19}$$

2.1.5 Fluctuation Dissipation Theorem in Stokes Flow

In Chapter 5, thermal fluctuations are included into the Newtonian stress tensor in order model a thermally perturbed thin liquid film. The magnitude of these fluctuations is set such that equipartition of thermal energy is maintained in all degrees of freedom. Such a restriction leads to a connection between the linear dissipation of a system that obeys a linear stochastic differential equation of the form (2.15).

In order to include a stochastic term into the Stokes equation, it must first be assumed that each fluid element is in local equilibrium with a temperature T.[9] Although the analysis here is built upon the assump-

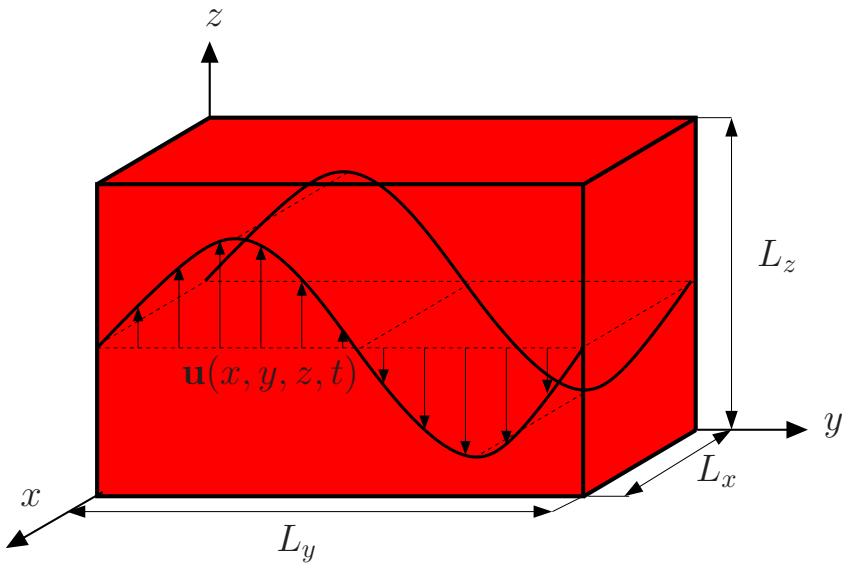

Figure 2.1: Periodic image of bulk fluid domain with periods of L_x, L_y, and L_z. Fluid velocity profile is described as $\mathbf{u}(x, y, z, t)$.

tion that the fluid particle is in equilibrium with no external forces, results of this analysis are often extended into non-equilibrium flows[32] that are in local equilibrium. This extension of equilibrium results into non-equilibrium flows is based upon the assumption that the procedure of including local fluctuations about non-equilibrium fluid flows is identical to including fluctuations about equilibrated flow.[32] This assumption of local equilibrium allows the results from equilibrium statistical mechanics to be applied to non-equilibrium flows, by applying the equipartition theorem to non-equilibrated problems by including $k_B T/2$ of thermal energy in perturbations about the non-equilibrium flow profile,[32] where k_B is Boltzmann's constant.

Beginning with continuum fluid particle, the volume specific momentum equation is

$$\rho \frac{\partial u_i}{\partial t} = -\frac{\partial p}{\partial x_i} + \frac{\partial T'_{ij}}{\partial x_j}, \tag{2.20}$$

where $\frac{\partial u_i}{\partial t}$ is ith component of the velocity, t is time, T'_{ij} the stress tensor, and ρ is the density of the fluid. Modeling the fluid as Newtonian with thermal fluctuations,

$$T'_{ij} = \eta \left(\frac{\partial u_i}{\partial x_j} + \frac{\partial u_j}{\partial x_i} \right) + \beta \mathcal{S}_{ij}, \tag{2.21}$$

with η the Newtonian shear viscosity and β' the magnitude of the stochastic fluctuations. $\mathcal{S}_{ij}$ is the normalized random forcing term (modeled as a Gaussian white noise) and is a function of position $\mathbf{r}$ and time t with an ensemble average of zero

$$\langle \mathcal{S}_{ij}(\mathbf{r},t)\rangle = 0, \tag{2.22}$$

and an autocorrelation

$$\langle \mathcal{S}_{ij}(\mathbf{r},t)\mathcal{S}_{lm}(\mathbf{r}',t')\rangle = (\delta_{il}\delta_{jm}+\delta_{im}\delta_{jl})\delta(t-t')\delta(\mathbf{r}-\mathbf{r}'). \tag{2.23}$$

Assuming a periodic fluid domain, as shown in Figure 2.1 with periods of L_x, L_y, and L_z in the respective x, y, and z directions, we can decompose the flow variables into their Fourier modes, such that any function $f(\mathbf{r},t)$ is

$$f(\mathbf{r},t) = \sum_{\mathbf{k}} \hat{f}(\mathbf{k},t)e^{i\mathbf{k}\cdot\mathbf{r}} \tag{2.24}$$

which is a sum over all the wavevectors of the periodic image such that

$$\mathbf{k} = \left(\frac{2\pi n}{L_x}, \frac{2\pi m}{L_y}, \frac{2\pi l}{L_z}\right), \tag{2.25}$$

and m, n, and l are integers.

Because we are attempting to find the amplitude of the fluctuations about an equilibrium state, where we can employ equipartition, the pressure gradients are zero, $\frac{\partial p}{\partial x_i} = 0$. By transforming the Navier–Stokes equation (2.58) via (2.24) and assuming a stress tensor of the form (2.21),

$$\rho\frac{\partial \hat{u}_i}{\partial t} = -|k^2|\eta\hat{u}_i + i\beta k_j\hat{\mathcal{S}}_{ij}, \tag{2.26}$$

which is simply an O-U model process. Thus from (2.16), we know the ensemble averaged, mean-square magnitude of $\hat{u}_i$ is

$$\langle \hat{u}_i^2\rangle = \frac{\beta^2}{2\eta\rho}. \tag{2.27}$$

Assuming that there is $k_BT/2$ of energy in each degree of freedom, as re-

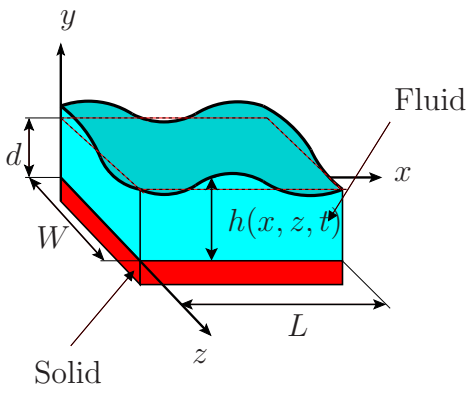

Figure 2.2: Domain schematic.

quired by equipartition, then

$$\langle \hat{u}_i^2 \rangle = \frac{k_B T}{\rho}, \tag{2.28}$$

which when combined with (2.27), the magnitude β is found to be

$$\beta = \sqrt{2\eta k_B T}. \tag{2.29}$$

This result for the magnitude of the thermal fluctuations within the stochastic stress tensor is equivalent to the results originally derived by Landau and Lifshitz.[13]

2.2 Decay Rates of Thermal Capillary Waves

In Chapter 4 we examine the dynamics of thermal capillary waves relaxing upon thin film interfaces. The system studied is designed so that the thermal capillary waves perturb the stable thickness of the liquid film, as shown schematically in Figure 2.2. For convenience the system is assumed to be periodic in both the x and z directions with periods of L and W, respectively. The fluid is assumed to have constant surface tension γ and viscosity η. Its local thickness is $y = h(x, z, t)$. Neglecting any gas-phase dynamics and assuming a small free-surface slope, the Laplace pressure on

the liquid side of the interface simplifies to

$$p(x,z,t) = -\gamma \nabla_{2D}^2 h(x,z,t), \tag{2.30}$$

where ∇_{2D}^2 is the two-dimensional Laplacian in x and z. The surface energy fluctuations associated with the thermal deformation of the free surface satisfy

$$\langle E - \langle E \rangle \rangle = \frac{1}{2} k_B T \tag{2.31}$$

for each degree of freedom, where k_B is the Boltzmann constant and T is the temperature of the fluid. The energy of a perturbation is the change in interface surface area due to that perturbation multiplied by the surface tension γ,

$$\langle E - \langle E \rangle \rangle = \left\langle \gamma \int_0^L \int_0^W \sqrt{1 + |\nabla h|^2} \mathrm{d}x \mathrm{d}z \right\rangle - \gamma LW. \tag{2.32}$$

The film thickness is decomposed into Fourier modes as

$$h(\mathbf{r},t) = \sum_{\mathbf{q}} h_{\mathbf{q}}(t) \exp(i\mathbf{q} \cdot \mathbf{r}), \tag{2.33}$$

where $\mathbf{r}$ is a position vector in the x–z plane and $\mathbf{q}$ is the corresponding two-dimensional wavenumber. The sum is over all $\mathbf{q}$ such that

$$\mathbf{q} = \left(\frac{2\pi n_x}{L}, \frac{2\pi n_z}{W} \right), \tag{2.34}$$

with n_x and n_z integers. Thus, from (2.31), (2.32) and (2.33) the mean squared amplitude of each Fourier coefficient $h_{\mathbf{q}}(t)$ must satisfy

$$\langle h_{\mathbf{q}}^2 \rangle = \frac{k_B T}{\gamma LW |\mathbf{q}^2|}, \tag{2.35}$$

so long as γ is constant and interface deformations are small.

The dynamics of a thermal mode is only a function of the magnitude of its wavenumber, so the following simplified analysis in two dimensions extends directly to three dimensions. We start with the Stokes equation,

$$\eta \nabla^2 \mathbf{v} = \nabla p, \tag{2.36}$$

where $\mathbf{v}$ is velocity and p is the pressure. This zero-Reynolds-number approximation will be satisfied by all perturbations considered in Section 4.3. Taking the curl of (2.36) and decomposing $\mathbf{v}$ as

$$\mathbf{v}(x, y, t) = \tilde{\mathbf{v}}(q, y, \omega) \exp(iqx - \omega t) \tag{2.37}$$

yields

$$[\partial_y^2 - q^2]\tilde{\mathbf{\Omega}}(q, y, \omega) = 0, \tag{2.38}$$

where $\tilde{\mathbf{\Omega}}(q, y, \omega) \equiv \nabla \times \tilde{\mathbf{v}}(q, y, \omega)$ has a non-zero value only in the z-component, for which the solution is

$$\tilde{\Omega}_z(q, y, \omega) = A \cosh(qy) + B \sinh(qy), \tag{2.39}$$

where A and B the undetermined constants.

Applying the incompressibility constraint $\nabla \cdot \mathbf{v} = 0$, which corresponds to

$$\tilde{v}_x(q, y, \omega) = \frac{i}{q} \frac{\partial}{\partial y} \tilde{v}_y(q, y, \omega), \tag{2.40}$$

yields

$$\tilde{\Omega}_z(q, y, \omega) = \frac{i}{q} \frac{\partial^2}{\partial y^2} \tilde{v}_y(q, y, \omega) - iq\tilde{v}_y(q, y, \omega). \tag{2.41}$$

Applying (2.39) and solving yields

$$\tilde{v}_y(q, y, \omega) = C_1 \cosh(qy) + C_2 \sinh(qy) + C_3 qy \cosh(qy) + C_4 qy \sinh(qy), \tag{2.42}$$

where A and B are now incorporated into C_1 through C_4, which are also are undetermined constants. The pressure is found from (2.36) and (2.74) to be

$$\tilde{p}(q, z, \omega) = \frac{1}{q^2} \left[\frac{\partial^3}{\partial y^3} \tilde{v}_y(q, y, \omega) - q^2 \frac{\partial}{\partial y} \tilde{v}_y(q, y, \omega) \right]. \tag{2.43}$$

The boundary conditions fix C_1 through C_4. The usual no-slip, no-penetration conditions at the wall are

$$\tilde{\mathbf{v}}_q(y = 0) = 0, \tag{2.44}$$

and the zero-shear-stress condition at the free surface is

$$\mathbf{t} \cdot \tau \cdot \mathbf{n} = 0, \tag{2.45}$$

where $\mathbf{t}$ and $\mathbf{n}$ are the interface tangent and normal vectors and τ_{ij} is the Newtonian-fluid stress tensor

$$\tau_{ij} = \eta \left(\frac{\partial v_i}{\partial x_j} + \frac{\partial v_j}{\partial x_i} \right) + \delta_{ij} p. \tag{2.46}$$

By assuming that the amplitude of the perturbation is small relative to either the wavelength of the surface perturbation or thickness of the film ($h_q \ll d$ within the long-wavelength lubrication regime, and $h_q \ll 1/q$ in the thick film regime), the leading order form of (2.45) is

$$\tau_{12}(y = d) = 0. \tag{2.47}$$

The normal stress condition matches the Laplace pressure

$$\mathbf{n} \cdot \tau \cdot \mathbf{n} = \gamma \kappa, \tag{2.48}$$

with κ the local curvature. This condition linearizes to

$$\tau_{22}(y = d) = \gamma q^2 h_q(\omega). \tag{2.49}$$

Linearization of the kinematic free-surface condition yields

$$\tilde{v}_y(y = d) = -\omega h_q(\omega). \tag{2.50}$$

Applying (2.44), (2.47) and (2.50) to (2.42) yields the relaxation rate

$$\omega(q) = \frac{\gamma q^2}{\eta B(q)}, \tag{2.51}$$

where

$$B(q) = 4q \frac{\cosh^2(qd) + q^2 d^2}{\sinh(2qd) - 2qd}. \tag{2.52}$$

There are two obvious asymptotic limits of this expression

$$\omega(q) = \begin{cases} \frac{\gamma d^3}{3\eta} q^4 & qd \ll 1 \\ \frac{\gamma}{2\eta} q & qd \gg 1. \end{cases} \tag{2.53}$$

Clearly, $\omega(q) \sim q^4$ corresponds to the long-wavelength lubrication regime while $\omega(q) \sim q$ corresponds to thick films. These are expected to fail as d or disturbances wavelengths $2\pi/q$ approach molecular dimensions. The height-height correlations of the Fourier modes of our fluid interface are measurable in our molecular simulations. The expected behavior of the correlations can be constructed by renaming $\tilde{v}(y = d) = \frac{\mathrm{d}h_q(t)}{\mathrm{d}t}$, which implies via (2.50)

$$\frac{\mathrm{d}h_q(t)}{\mathrm{d}t} = -\omega(q) h_q(t). \tag{2.54}$$

Including a stochastic noise term into each mode to account to model thermal fluctuations, and multiplying by $\mathrm{d}t$,

$$\mathrm{d}h_q(t) = -\omega(q) h_q(t)\mathrm{d}t + \beta \mathrm{d}B_t, \tag{2.55}$$

which is the stochastic differential equation of an O-U process, where β is the magnitude of the thermal fluctuations. As demonstrated in Section 2.1.4,

$$\langle h_q(0) h_q(t) \rangle = \langle h_q^2 \rangle e^{-\omega(q)t}. \tag{2.56}$$

and via the results of equipartition (2.35),

$$\langle h_q(0) h_q(t) \rangle = \frac{k_B T}{\gamma L W |q^2|} e^{-\omega(q)t}. \tag{2.57}$$

2.3 Thermally Driven Interface Dynamics

Following the development of a stochastic lubrication equation by Grun *et al.*,[10] a thermally augmented lubrication equation can be developed by adding a stochastic stress term $\nabla \cdot \mathcal{S}$ to the Navier–Stokes equation, where $\mathcal{S}$ is a stochastic stress tensor of normalized Gaussian white noise components. The coefficient in front of this stress tensor, β will be set based upon the fluctuation–dissipation theorem, as discussed in Section 2.1.5.

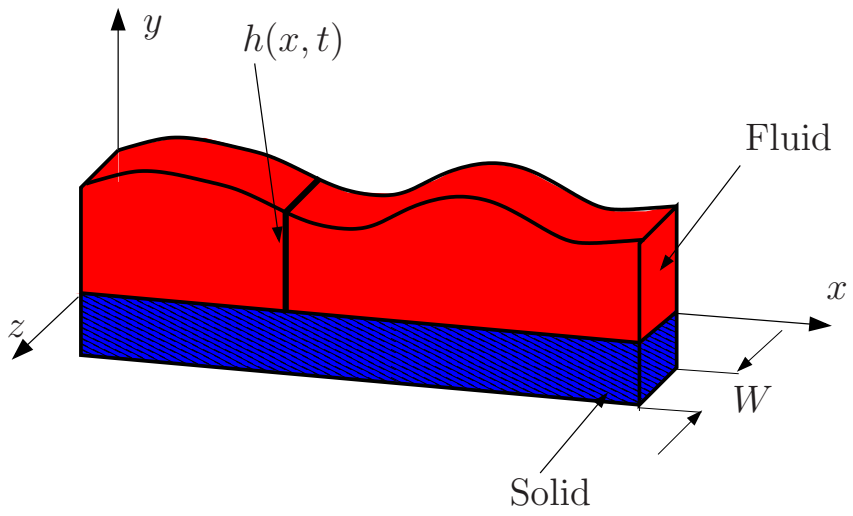

Figure 2.3: Domain of stochastic evaporating lubrication equation. Domain has been averaged in the z direction and has a fixed width of W. Interface height at position x and time t is labeled as $h(x,t)$.

This term models the stochastic stresses associated with the thermal fluctuations:

$$\rho\frac{D\mathbf{u}}{Dt} = -\nabla p + \eta\nabla^2\mathbf{u} + \beta\nabla\cdot\mathcal{S}. \tag{2.58}$$

As shown in Figure 2.3, the domain is averaged in the z direction for a domain of width W, reducing our representation of the interface to a one dimensional curve, $h(x,t)$. When averaged over a width of W, the magnitude of the stochastic fluctuations (2.29) becomes

$$\beta = \sqrt{\frac{2\eta k_B T}{W}}. \tag{2.59}$$

This two-dimensional stress stochastic stress has zero mean $\langle\mathcal{S}\rangle = 0$ with an autocorrelation value of

$$\langle\mathcal{S}_{ij}(x,y,t)\mathcal{S}_{kl}(x',y',t')\rangle = \delta(x-x')\delta(y-y')\delta(t-t')(\delta_{il}\delta_{jm}+\delta_{im}\delta_{jl}). \tag{2.60}$$

Assuming an incompressible fluid, the continuity constraint becomes

$$\nabla\cdot\mathbf{u} = 0, \tag{2.61}$$

with $\mathbf{u} = [u, v]$, the x and y components of the velocity. Letting the fluid be Newtonian, the elements of the viscous stress tensor $\mathbf{T}$ are defined as

$$T_{ij} = \eta \left(\frac{\partial u_i}{\partial x_j} + \frac{\partial u_j}{\partial x_i} \right) + p\delta_{ij}, \tag{2.62}$$

with η being the Newtonian shear viscosity, and p the fluid pressure. The boundary conditions of this problem at the liquid–solid interface at $y = 0$ are no-slip, no-penetration,

$$u = 0 \quad \text{and} \quad v = 0, \tag{2.63}$$

respectively. At the liquid–vapor interface, the full normal stress and tangential stress are balanced by the Laplace pressure and the vapor pressure,

$$(\mathbf{T} + \mathcal{S}) \cdot \mathbf{n} = (\gamma\kappa - p_v)\mathbf{n}, \tag{2.64}$$

with γ the surface tension, κ the local curvature and p_v the vapor pressure.

2.3.1 Evaporation

Low molecular weight polymers are used in the simulations to be discussed in Chapters 4 and 5. These have the advantage of having a relatively low liquid-state viscosity, which increases the rate of spreading and thereby increases the scope of this study. However, the fluid used in the spreading drop (Chapter 5) has a non-negligible evaporation, which must be included in our thin-film model. The model we employ uses the linearized non-equilibrium evaporation model of Schrage,[33] which has been used to study the dynamics of small confined bubbles[29] as well as an atomistic meniscus.[11] In this model, the mass flux of evaporation J^* is linearly proportional to the pressure jump across the interface

$$J^* = \rho_v \left(\frac{2\pi}{\bar{R}T^i} \right)^{1/2} \left(\frac{p_v^e}{p_v} - 1 \right), \tag{2.65}$$

with ρ_v the vapor density, $\bar{R}$ the mass-specific gas constant, T^i the temperature at the fluid-vapor interface, and p_v^e and p_v the equilibrium vapor pressure and local pressure at the interface, respectively.

For non-dimensionalization, we follow Ajaev & Homsy[29] and define velocity and pressure scales

$$U = \frac{kT_s^*}{\rho \mathcal{L} l} \quad \text{and} \qquad p = \tfrac{\gamma}{l}, \tag{2.66}$$

with k the thermal conductivity of the fluid, $\mathcal{L}$ the latent heat of vaporization, T_s the equilibrium saturation temperature, ρ the liquid density, and l an appropriate macroscopic length scale, which we take to be the x-domain length of the simulation. With these, the non-dimensional mass flux is

$$J = \frac{\delta_v(p - p_v) + T^i - 1}{K}, \tag{2.67}$$

where

$$K = \frac{\rho U \sqrt{2\pi T_s}}{2\rho_v \mathcal{R}} \qquad \text{and} \qquad \delta_v = \frac{\gamma}{\rho \mathcal{L} l}, \tag{2.68}$$

with $\mathcal{R}$ the specific gas constant for our fluid. As explained by Ajaev *et al.*,[29] K represents the relative importance of kinetic effects in changing local vapor pressure and δ_v relates the change in local pressure of the liquid to changes in local evaporation temperature.

Furthermore, the energy balance across the evaporating interface is enforced via a constraint upon the temperature gradient ∇T with

$$J = -\mathbf{n} \cdot \nabla T, \tag{2.69}$$

while T the temperature of the fluid, is also assumed to be quasi-static, namely

$$\nabla^2 T = 0. \tag{2.70}$$

2.3.2 Capillary scaling

To balance the effects of pressure driven flow, evaporation, and thermally driven flow, we applied the scalings of Ajaev & Homsy,[29]

$$\begin{aligned} x &= Ca^{1/6} l\hat{x}, & y &= Ca^{1/3} l\hat{y}, & h &= Ca^{1/3} l\hat{h}, \\ t &= Ca^{2/3}\frac{l}{U}\hat{t}, & u &= Ca^{-1/2} U\hat{u}, & v &= Ca^{-1/3} U\hat{v}, \\ J &= Ca^{-1/3}\hat{J}, & K &= Ca^{1/3}\hat{K}. \end{aligned}$$

To retain the stochastic stresses in the $Ca \to 0$ limit we similarly choose

$$\beta = Ca^{-1/4}\hat{\beta}. \tag{2.71}$$

These choices lead to simplifications of the general equations such that the Navier-Stokes momentum equations (2.58) reduce to

$$-\frac{\partial \hat{p}}{\partial \hat{x}} + \frac{\partial^2 \hat{u}}{\partial \hat{y}^2} + \hat{\beta}\frac{\partial \hat{\mathcal{S}}_{12}}{\partial \hat{y}} = 0 \qquad \text{(x-momentum)} \tag{2.72}$$

$$-\frac{\partial \hat{p}}{\partial \hat{y}} = 0 \qquad \text{(y-momentum)}, \tag{2.73}$$

while the continuity equation (2.61) remains as

$$\frac{\partial \hat{u}}{\partial \hat{x}} + \frac{\partial \hat{v}}{\partial \hat{y}} = 0. \tag{2.74}$$

$\mathcal{S}_{12}$ is the shear-stress component of the stochastic stress tensor $\mathcal{S}$. Under these capillary scalings, the fluid-vapor interface boundary conditions (2.64) reduce to

$$-p = \frac{\partial^2 \hat{h}}{\partial \hat{x}^2} - p_v \qquad \text{(normal stress)} \tag{2.75}$$

$$\frac{\partial \hat{u}}{\partial \hat{y}} + \hat{\beta}\hat{\mathcal{S}}_{12} = 0 \qquad \text{(shear stress)}. \tag{2.76}$$

In this limit of the flow equation, the stochastic contribution only appears in the tangential stress at the interface, while the normal stochastic stress is not of the same order as the surface tension and vapor pressure. Because the thermal fluctuations only play a role in the tangential

stresses of our model and not in the local normal pressure, the evaporation model (2.67) shows that thermal fluctuations have no direct effect upon evaporation in this small capillary number scaling. In the full solution of the Navier–Stokes equations, the stochastic term would alter the local surface pressure and thus effect evaporation dynamics. However, as will be shown in Section 2.3.4, this stochastic contribution to evaporation can be approximated and it will be verified that the stochastic contributions to evaporation are negligible for the drop of Chapter 5.

The capillary scaling also reduces the evaporation energy balance (2.69) to

$$\hat{J} = -\frac{\partial \hat{T}}{\partial \hat{y}}, \tag{2.77}$$

and (2.70) is simplified to

$$\frac{\partial^2 \hat{T}}{\partial \hat{y}^2} = 0. \tag{2.78}$$

2.3.3 The Stochastic Evaporating Lubrication Equation

The velocity in the x-direction, u, can be found by integrating (2.72) and applying the no-slip boundary condition as well as the stochastic free interface boundary condition (2.76):

$$\hat{u} = \frac{\partial \hat{p}}{\partial \hat{x}} \left(\frac{\hat{y}^2}{2} - \hat{h}\hat{y} \right) - \hat{\beta} \int_0^{\hat{y}} \hat{\mathcal{S}}_{12} \mathrm{d}\hat{y}. \tag{2.79}$$

Applying the continuity equation (2.74) to (2.79), along with the no-penetration condition (2.63), yields

$$\hat{v} = \frac{\partial}{\partial \hat{x}} \left[\frac{\partial \hat{p}}{\partial \hat{x}} \left(\frac{\hat{y}^3}{6} - \frac{\hat{h}\hat{y}^2}{2} \right) - \hat{\beta} \int_0^{\hat{y}} \int_0^{\hat{y}'} \hat{\mathcal{S}}_{12} \mathrm{d}\hat{y}' \mathrm{d}\hat{y} \right]. \tag{2.80}$$

Using integration by parts on the last term of (2.80) and substituting it in with the expression for the x-velocity (2.79) into the scaled kinematic condition

$$\hat{J} = -\hat{u}\frac{\partial \hat{h}}{\partial \hat{h}} + \hat{v} - \frac{\partial \hat{h}}{\partial \hat{t}}, \tag{2.81}$$

the evaporating stochastic lubrication equation becomes

$$\frac{\partial \hat{h}}{\partial \hat{t}} = \frac{\partial}{\partial \hat{x}} \left[\hat{h}^3 \frac{\partial \hat{p}}{\partial \hat{x}} - \hat{\beta} \int_0^h (h - \hat{y}) \hat{\mathcal{S}} \mathrm{d}\hat{y} \right] - \hat{J}. \tag{2.82}$$

However, the existence of an integral in the stochastic term is not convenient for analysis. Grun *et al.*[10] demonstrated the existence of a simpler version of this stochastic term that has an equivalent probability distribution where

$$\frac{\partial \hat{h}}{\partial \hat{t}} = \frac{\partial}{\partial \hat{x}} \left[\hat{h}^3 \frac{\partial \hat{p}}{\partial \hat{x}} - \hat{\beta} \sqrt{\frac{\hat{h}^3}{3}} \mathcal{N} \right] - \hat{J}, \tag{2.83}$$

where the two-dimensional noise term $\mathcal{S}_{12}(x, y, t)$ has been reduced to a more tractable one-dimension term $\mathcal{N}(x, t)$ with expectation and autocorrelation properties of

$$\langle \mathcal{N}(x, t) \rangle = 0 \quad \text{and} \quad \langle \mathcal{N}(x', t') \mathcal{N}(x, t) \rangle = \delta(x' - x) \delta(t' - t). \tag{2.84}$$

The $J = 0$ version of (2.83) is identical to the stochastic lubrication equation derived by Davidovitch *et al.*[9] and Grun *et al.*[10] In order to solve for the evaporation, the x-velocity, (2.79) can be substituted into the scaled heat equation (2.78) as well as the interface energy balance (2.69) to arrive fluid interface temperature,

$$T_i = T(h) = -\hat{J}\hat{h} + T_w. \tag{2.85}$$

This can then be included into the non-equilibrium condition model (2.67), which when scaled yields

$$\hat{J} = \frac{\delta(\hat{p} - \hat{p}_v) + T_w - 1}{\hat{K} + \hat{h}}. \tag{2.86}$$

By including assumptions particular to our molecular spreading drop, the resulting lubrication equation becomes

$$\frac{\partial \hat{h}}{\partial \hat{t}} = \frac{\partial}{\partial \hat{x}} \left[\underbrace{-\hat{h}^3 \frac{\partial^3 \hat{h}}{\partial \hat{x}^3}}_{\text{Lubrication}} + \underbrace{\hat{\beta} \hat{h}^{3/2} \mathcal{N}(\hat{x}, \hat{t})}_{\text{Stochastic}} \right] + \underbrace{\frac{\delta_v \frac{\partial^2 \hat{h}}{\partial \hat{x}^2}}{\hat{K} + \hat{h}}}_{\text{Evaporative}}, \tag{2.87}$$

where the terms on the right-hand side correspond respectively to the lubrication dynamics (an interplay of viscous and surface forces) , thermal fluctuations, and evaporation of the film. Equation (2.87) is simplified by several assumptions, the first being that the saturation temperature is equivalent to the wall temperature. This assumption is justified given that our simulation domain is essentially isothermal, with the temperature maintained by using a weak stochastic thermostat on the solid wall. This will be confirmed by measuring thermal gradients within the domain. No thermal gradients are expected, given the fact the $\hat{K}$ is approximately 400 times greater than $\hat{h}$ for precursor film, which essentially minimizes thermal gradients for the majority of the surface area of the fluid interface. A second assumption is that there is no disjoining pressure contribution from van der Waals or any other forces. This assumption will be discussed in section 3.2.4.

2.3.4 Violation of the Fluctuation-Dissipation Theorem

Another key point that must be addressed is that (2.87) does not formally obey the fluctuation-dissipation theorem. The fluctuation-dissipation theorem relates the energy of fluctuations of a system to the energy dissipated by an infinitesimal external perturbation of the system, yielding in the equations of motion a fluctuation term with a magnitude proportional to the square root of the linearized dissipative term. However (2.87) only contains the fluctuations from the interaction with viscous dissipation, without accounting for the fluctuations associated with the evaporative dissipation. To justify this we linearized the deterministic dimensional version of (2.87) for a single wavenumber component q by making the substitution

$$h(x,t) = H + \delta h(t)\cos(qx). \tag{2.88}$$

Assuming that $H \gg \delta h(t)$, leads to

$$\frac{\partial \delta h(t)}{\partial t} = \left(- \underbrace{\frac{H^3 \gamma q^4}{\eta}}_{\text{Viscous}} - \underbrace{\frac{2kT_s \rho_v \gamma \mathcal{R} q^2}{\rho^2 \mathcal{L}(k\sqrt{2\pi}T_s^{3/2} + 2H\mathcal{L}\mathcal{R}\rho_v)}}_{\text{Evaporative}} \right) \delta h(t), \qquad (2.89)$$

and we compare the relative importance of the viscous versus evaporative dissipation terms by substituting values of q and H corresponding to the length and thickness of the drop. This long-wavelength choice for q, maximizes the relative importance of the evaporation dissipation. Substituting these values and the physical properties of the liquid – measured using the techniques explained in Chapter 3 and listed in Table 5.1– into the two linear dissipation terms of (2.89) suggests the viscous dissipation term is 1.8×10^6 larger than the evaporative dissipation. Thus because the magnitude of the fluctuations in this linear model is proportional to the square root of the dissipation term, the viscous fluctuation is expected to be over 1000 times greater than the evaporative fluctuation term, justifying its neglect in the current study. Although the fluctuating evaporation is negligible, evaporation itself is still important due to local variations in pressure because of the interface curvature, and this is accounted for in (2.86).

2.4 Predictions of Enhanced Spreading of a Droplet Due to Thermal Fluctuations

In Chapter 5, the spreading rate of a molecular drop is compared to the predictions of (2.83) with and without thermal noise. The motivation for this test is to assess both whether thermal fluctuations do enhance spreading as predicted by Davidovitch *et al.*,[9] as well the applicability of a stochastic continuum model (2.83) to molecular fluid behavior. The arguments of Davidovitch *et al.* [9] are expressed here.

Starting with the $J = 0$ version of (2.87),

$$\frac{\partial \hat{h}}{\partial \hat{t}} = \frac{\partial}{\partial \hat{x}} \left[\underbrace{-\hat{h}^3 \frac{\partial^3 \hat{h}}{\partial \hat{x}^3}}_{\text{Laplace Pressure}} + \underbrace{\hat{\beta} \hat{h}^{3/2} \mathcal{N}(\hat{x}, \hat{t})}_{\text{Stochastic}} \right], \tag{2.90}$$

Davidovitch *et al.*[9] suggested that as there exists both a Laplace pressure driven regime, often know as Tanner's law,[34] and a regime where the stochastic forcing dominates in which the Laplace pressure from the surface tension can be neglected. Laplace pressure dominated flows are thus described by only the first term of (2.90),

$$\frac{\partial \hat{h}}{\partial \hat{t}} = \frac{\partial}{\partial \hat{x}} \left[-\hat{h}^3 \frac{\partial^3 \hat{h}}{\partial \hat{x}^3} \right], \tag{2.91}$$

and the stochastic dominated regime by the second term,

$$\frac{\partial \hat{h}}{\partial \hat{t}} = \frac{\partial}{\partial \hat{x}} \left[\hat{\beta} \hat{h}^{3/2} \mathcal{N}(\hat{x}, \hat{t}) \right]. \tag{2.92}$$

Davidovitch *et al.*[9] postulated that each equation, (2.91) and (2.92) will admit self-similar solutions of the form

$$h(x, t) = \frac{f(x/t^z)}{x}, \tag{2.93}$$

where z is an adjustable variable. By making a similarity transform

$$x \to bx, \quad h \to h/b, \quad \text{and} \quad t \to b^z t, \tag{2.94}$$

and substituting these into (2.92) and (2.93),

$$b^{-1-z} \frac{\partial \hat{h}}{\partial \hat{t}} = b^{-1} \frac{\partial}{\partial \hat{x}} \left[-b^{-3} \hat{h}^3 b^{-4} \frac{\partial^3 \hat{h}}{\partial \hat{x}^3} \right], \tag{2.95}$$

for the Laplace pressure driven interface and

$$b^{-1-z} \frac{\partial \hat{h}}{\partial \hat{t}} = b^{-1} \frac{\partial}{\partial \hat{x}} \left[\hat{\beta} b^{-3/2} \hat{h}^{3/2} b^{-1/2-z/2} \mathcal{N}(\hat{x}, \hat{t}) \right], \tag{2.96}$$

for the stochastic driven interface. In order for the similarity transforms to

hold true, $z = 7$ in (2.95), while $z = 4$ in (2.96), which implies two power-law spreading regimes,

$$x \sim t^{1/7} \qquad \text{Tanner's Law, and} \tag{2.97}$$

$$x \sim t^{1/4} \qquad \text{Stochastic spreading.} \tag{2.98}$$

The $t^{1/4}$ spreading rate of the stochastic dominated spreading suggests that when a fluid is in the stochastic regime it should spread faster than Tanner's law of $x \sim t^{1/7}$. This new, enhanced spreading rate can be expected when the Laplace pressure term (2.91) is much less than the stochastic forcing term (2.92),

$$\frac{\partial}{\partial \hat{x}}\left[-\hat{h}^3\frac{\partial^3 \hat{h}}{\partial \hat{x}^3}+\right] \ll \frac{\partial}{\partial \hat{x}}\left[\hat{\beta}\hat{h}^{3/2}\mathcal{N}(\hat{x},\hat{t})\right]. \tag{2.99}$$

This inequality suggest that stochastic dominated spreading will occur when

$$|x| \gg x^* \quad \text{and} \quad h \ll h_o^2/x^*, \tag{2.100}$$

where $x^* = \frac{h_o^{7/6}W^{1/6}}{l_T^{1/3}}$, h_o the initial drop height, W the width of the homogenized domain, and l_t is the thermal length scale (1.1). Intuitively, for a drop to enter this stochastic regime, it must be able to become sufficiently flat that its curvature is reduced to a point where the Laplace pressure is negligible when compared to the temperature dependent stochastic stress.

Chapter 3

Computational Methods

3.1 Molecular Modeling

In order to test the predictions of continuum modeling at length scales where thermal fluctuations affect mechanics, we employed molecular simulations as our "experimental" fluid. This molecular fluid was built using a convenient, yet realistic, model of simple fluid atoms based upon the Lennard–Jones pair potential, explained in Section 3.1.1. However, because of the relative volatility of a simple Lennard–Jones fluid, we included a polymer model to link atoms in chains and thereby reduce evaporation, as discussed in Section 3.1.2. The model fluid molecules were then placed in a periodic computational domain, discussed in Section 3.1.3, and allowed to equilibrate onto a crystal substrate. Taking advantage of the periodicity of our simulation domain, Section 3.1.4 describes how the initial conditions for molecular dynamics simulations were constructed.

3.1.1 Lennard–Jones Pair Potential

In all of our simulations, atoms interact via the Lennard–Jones potential,[12] u_{LJ}. This model employs an attractive potential ($1/r^6$) and an empirical repulsion ($1/r^{12}$) with

$$u_{LJ}(r) = 4\varepsilon \left[\frac{\sigma^6}{r^6} - \frac{\sigma^{12}}{r^{12}} \right], \tag{3.1}$$

σ the collision length scale, ε the energy of interaction between two atoms, and r the radial distance between two atoms. The $1/r^6$ models the attractions of two non-polar atoms due to instantaneous dipole fluctuations, while the $1/r^{12}$ is an empirical approximation to the repulsion energy of

two non-polar atoms.[12] Because of the decay of both the attractive and repulsive terms, the computational cost of force calculations can be reduced by introducing a truncation length into (3.1), as discussed in Section 3.2.3.

Despite being a very simple model of inter-atomic energies, the Lennard–Jones potential provides reasonable agreements with experimental properties of simple liquids, such as argon.[12] In order to facilitate dimensional comparisons, the Lennard–Jones parameters for our simulation were set at values shown to model liquid argon, as summarized in Table 3.1.

Symbol	Description	Value
m	atom mass	6.6385×10^{-26}kg
ϵ/k_B	Lennard–Jones interaction energy	118K
σ	Lennard–Jones length scale	3.405×10^{-10}m

Table 3.1: Physical parameters used to model argon via (3.1).

3.1.2 Polymer Model

Given that the Lennard–Jones fluid represents only single atoms, it is limited in the range of fluids it can model. The relatively low critical temperature of the single atom fluid complicates interface dynamics by being prone to large amounts of evaporation which muddle the interpretation of molecular results. To avoid this problem, simple polymer models exist which model the basic features of more complex fluids.[35,36] At the temperatures of the simulations employed in both the spreading drop (Chapter 5) and the dynamics of thermal capillary waves (Chapter 4), these polymers have significantly less evaporation when compared to the single atom Lennard–Jones fluid. Because these coarse grained polymer models exhibit many of the features experimentally found in polymer flows, such as shear thinning, entanglement for larger polymers, and general changes in viscosity as a function of polymer molecule size,[36] the behaviors in this work should be generalizable to other fluids.

The polymer model used in our simulations, the finite extensible nonlinear elastic (FENE) potential, includes in addition to (3.1) an energy

of interaction between adjacent atoms within a single polymer:

$$u_{\mathrm{f}}(r) = \begin{cases} -\frac{1}{2}kR_o^2 \log\left[1 - \frac{r^2}{R_o^2}\right] & \text{for } r < R_o \\ \infty & \text{for } r \geq R_o, \end{cases} \tag{3.2}$$

with k and R_o the strength and length of the polymer bonds, respectively. The values of these parameters, shown in Table 3.2, were chosen to prevent bond crossings and be computationally efficient, as suggested by Kroger.[36]

Symbol	Description	Value
k	FENE spring constant	$30\frac{\varepsilon}{\sigma^2}$
R_o	FENE reference length	1.5σ

Table 3.2: Parameters for FENE polymer model in (3.2).

3.1.3 Domain

The simulation domain is periodic in all three spatial dimensions, as shown in Figure 3.1. The fluid molecules (red atoms) form a liquid film atop a solid substrate (white atoms), and the solid is attached to the rigid blue atoms. Each fluid atom has a mass of $m_f = m$ and the interaction energy between all fluid and solid atoms was the same: $\varepsilon_{ff} = \varepsilon_{sf} = \varepsilon$. The values of the molecular parameters were set to match that of liquid argon as listed in Table 3.1. As shown in Figure 3.1, the solid atoms in combination with the wall atoms were arranged into 4 layers of an FCC lattice. The mass and energy of the solid-solid interaction were set at $m_s = 10m$ and $\varepsilon_{ss} = 10\varepsilon$, which provided a melting temperature well above the temperatures used in our simulations, while still having vibration time scales that did not restrict the numerical time step of the velocity–Vertlet algorithm.

3.1.4 Initial Conditions

A significant amount of simulation time can be required to reach an equilibrium condition. To reduce this for our simulations we developed an efficient manner to produce almost equilibrated simulation domains. First, a small periodic sample of fluid of the desired polymer length is dispersed as

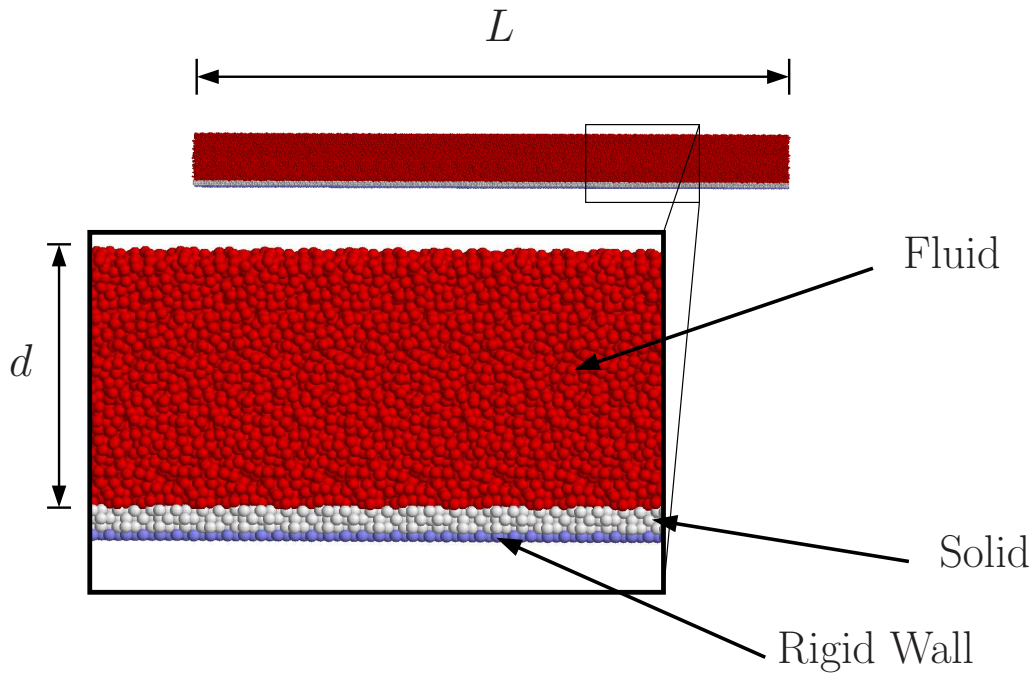

Figure 3.1: Two dimensional projection of three dimensional simulation domain with three types of atoms; rigid wall, frozen substrate, and fluid. The frozen substrate (white) and fluid atoms (red) are unconstrained and can move freely, while the wall atoms (blue) are held rigid. The domain is periodic in all three directions (including into the page). This film has a length of L and an average film thickness of d.

a gas in a tall rectangular domain and assigned velocities corresponding to high temperature ($\sim 500K$). Then applying a Bersenden thermostat[37] to the liquid atoms and an Andersen thermostat[38] to the wall atoms, the simulation is cooled down and allowed to condense upon the solid plate, which is held at the desired target temperature ($85 - 118K$). An example of this condensed film is shown in Figure 3.2(a). Most of the simulations discussed in this dissertation had temperatures set at $100K$. These small sample domains had a length and width of 6σ, while the height of the domain was chosen such that all the fluid atoms could be contained in the simulation domain. This height varied anywhere from 30σ to over 350σ depending on the required parameters of the initial condition. Once the sample had sufficient time to equilibrate, which was taken at the time when an average over 10^6 time steps the fluid of the simulation was within a 0.1 K of the set temperature and visual inspection of temperature profiles revealed no thermal gradients, the positions and velocities of the atoms were saved. These small simulation domains were then assembled to create the larger films, as shown in Figure 3.2(b). From this larger assembled domain, a desired initial profile of the liquid–vapor interface was cut out of the assembled film by removing all the atoms of all molecules that have a center of mass above the specified $h(x,t)$. This target shape is depicted with a black solid line in Figure 3.2(b). The final result is a semi-equilibrated profile in a specified shape, composed of a specified polymer, at specified temperature, as shown in Figure 3.2(c).

This interface of such a cut system is, of course, not exactly in a state of local equilibrium, which leads to a quick burst of evaporation, especially at the high curvature regions of the spreading drop (Chapter 5). As shown in Figure 3.3, during the first 2×10^7 of the 6×10^8 time steps, the character of the "length" (radius of gyration) of the fluid interface changed dramatically from a rapidly expanding evaporation regime to a slower spreading regime. At this point, the profile of the interface is defined as the initial condition of the spreading drop and data collection could begin to accumulate the statistics desired of the simulation.

This procedure of assembling larger domains from equilibrated smaller domains is an efficient manner to develop initial conditions for large variety of numerical experiments. Also such a standardized procedure allowed for

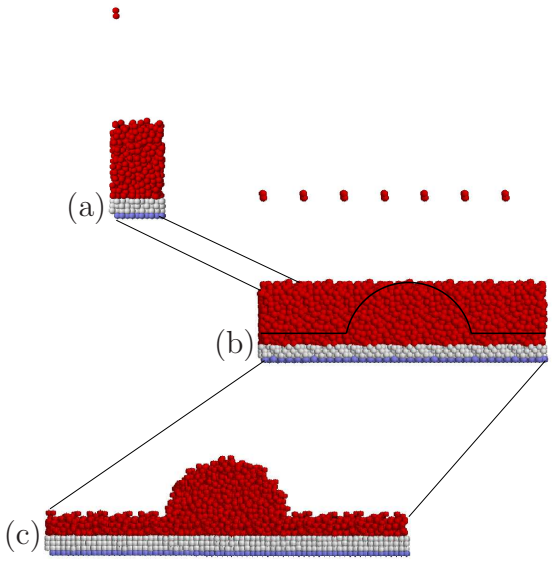

Figure 3.2: Shown is the process for constructing initial conditions for simulations. (a) Warm-up and equilibrate small sample of polymer fluid. (b) Assemble arbitrary domain shape from small fluid samples by fitting identical periodic boundaries adjacent to one another. The solid-black line represents the desired film profile $h(x,t)$. (c) Cut-out out desired film thickness and shape.

high precision control of the initial condition average film thickness for the large number of different types of fluids we compared in the capillary wave simulations of Chapter 4.

3.2 Molecular Dynamics Algorithms

Once an initial domain is defined and the atomic interactions model has been chosen, molecular motion is obtained by integrating the equations of motion for each atom within the simulations. The method of integration employed in our simulations of both Chapters 4 and 5 was the velocity-Vertlet integrator, discussed in Section 3.2.1. Although the velocity-Vertlet algorithm has excellent conservation properties, it is not perfect and the long time simulations ($\approx 10^8$ time steps) required the employment of several thermostats, as will be discussed in Section 3.2.2. Furthermore, be-

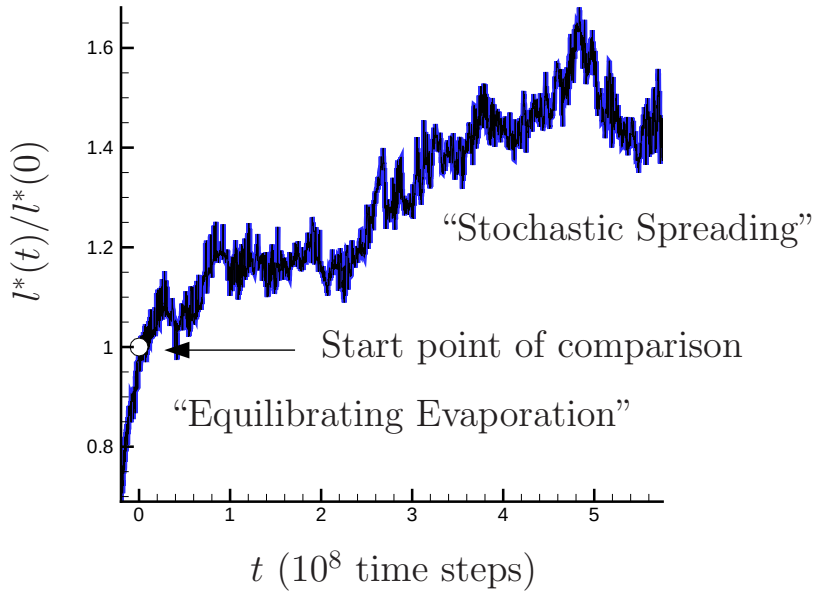

Figure 3.3: Radius of gyration of drop as a function of time. Shown is the choice of t=0, where the behavior of the drop changes from quick accumulation of fluid at the edge of boundaries because of "Equilibrating Evaporation" to the "Stochastic Spreading". At t=0, marked by the small open circle, the profile of the molecular simulation was exported for direct comparisons with solutions continuum models of interface dynamics.

cause of the relatively long times and large number of atoms ($\approx 10^5$) needed to make comparisons between atomic motion and continuum predictions, optimized numerical methods were required to make out molecular simulations tractable. One method employed for optimizing the force calculation included truncating the potential for atomic interactions in the simulated atoms, and taking advantage of the linear (with the number of atoms) computational cost of using neighborlists and link-cell binning, discussed in Section 3.2.3. Including truncation lengths into atomic interactions has implications when modeling thin films atop much thicker solid substrates, which is discussed in Section 3.2.4. Simulating polymers required additional modifications to neighborlists, which is discussed in Section 3.2.5. The large number of atoms in the molecular simulations required further optimization, where the workload of the simulations was distributed across many processors (16–128). The algorithm used to distribute the workload in an optimized manner is discussed in Section 3.2.6.

3.2.1 Integration

In simulating chaotic n-body particle systems, such as the atoms of our systems, it is impossible to accurately track the *exact* trajectory of the atoms. The slightest numerical error will grow exponentially in time. Fortunately, the reproducibility of molecular dynamics statistics between different realizations of the same simulations suggest that the statistics are insensitive to this, as argued by Rapaport.[39] For obtaining statistical results, it is more important to be sure the energy of the system is preserved. Symplectic integrators which by definition are canonical transformations and preserve volume in phase space, are therefore attractive. They have excellent conservation properties, preserving the time-reversible character of the governing equations, at least in the linear limit. It is for this reason that they are typically preferred over non-symplectic, though formally more accurate, methods such as high-order Runge–Kutta methods.[40]

The trajectories of all the atoms of our simulations are calculated using the velocity-Verlet integration scheme. This scheme has second-order accuracy, where error $\epsilon \sim \Delta t^3$ for time step Δt.[39] The velocity-Verlet integrator can be derived starting with an approximation of the future position

of a particle,

$$x(t_o + \Delta t) = x(t) + \Delta t \dot{x}(t_o) + \frac{\Delta t^2}{2}\ddot{x}(t) + O(\Delta t^3), \tag{3.3}$$

where $x(t_o)$ the position of particle at starting time t_o. By definition $\dot{x}(t) \equiv v(t)$ and Newton's second law gives that the acceleration of a particle of mass m is proportional to the force being applied $F(x(t))$ at $x(t)$. Thus

$$\dot{v}(t) = \frac{F(x(t))}{m}, \tag{3.4}$$

is substituted into (3.3) along with the definition of velocity, yielding the updated position

$$x(t_o + \Delta t) = x(t_o) + \Delta t v(t_o) + \frac{\Delta t^2}{2}\frac{F(x(t_o))}{m}. \tag{3.5}$$

In order to update the velocity at the next time step, $v(t_o + \Delta t)$ is approximated by

$$v(t_o + \Delta t) = v(t_o) + \Delta t \dot{v}(t_o) + \frac{\Delta t^2}{2}\ddot{v}(t_o) + O(\Delta t^3). \tag{3.6}$$

While Newton's second law (3.4) can replace $\dot{v}(t_o)$, $\ddot{v}(t_o)$ is approximated by

$$\ddot{v}(t_o) = \frac{\dot{v}(t_o + \Delta t) - \dot{v}(t_o)}{\Delta t} + O(\Delta t). \tag{3.7}$$

Applying (3.4) and (3.7) to (3.6) yields an approximation to update velocity, namely

$$v(t_o + \Delta t) = v(t_o) + \frac{F(x(t_o + \Delta t)) + F(x(t_o))}{2m} + O(\Delta t^3). \tag{3.8}$$

Thus the algorithm for time integration is as follows:

1. Calculate particle position $x(t_o + \Delta t)$ via (3.5).
2. Evaluate $F(x(t_o + \Delta t))$
3. Update particle velocity via (3.8).
4. Repeat steps 1–3

The standard practice within the literature, is to set the time steps for integration in molecular simulation of Lennard-Jones atoms as $\Delta t = .005\tau_{LJ}$, where $\tau_{LJ} = \sqrt{\frac{m\sigma}{\epsilon}}$ is the vibration timescale of Lennard-Jones atoms. Energy fluctuations were less than 4×10^{-5} of the total energy and energy loss was less than 4×10^{-5} energy loss over 10^5 time steps for a small simulation of 3732 Lennard–Jones atoms.

3.2.2 Thermostats

The velocity-Vertlet integration scheme used in the molecular simulations (Section 3.2.1) has excellent but not exact energy conservation, so we need to provide mild adjustments of temperature to conserve energy in the computational domain. We employed both an Andersen[38] thermostat as well as a Bersenden[37] thermostat to keep the computational domain at a constant temperature, but we do this in a way that causes little if any effect on the dynamics of the atoms in the system.

The approach of the Andersen thermostat is to in effect couple the system to a thermal reservoir at a specified temperature T. Unlike a Langevin[41] thermostat that includes a stochastic term into the equations of motion, Andersen thermostats only periodically modify the equations of motion for any atom by randomly selecting time steps during velocities of atoms are reassigned to mimic the effect of an impacting reservoir atom. The probability of an atom interacting with a reservoir atom and having its velocity reassigned is controlled by a parameter ν, which is set low such that stochastic intervention will on average take place once per Lennard–Jones vibrational time scale τ_{LJ}, $\nu = 0.005$. Although individual trajectories are modified, this thermostat, has been shown to produce ergodic trajectories[38] and reproduce statistics of a canonical ensemble.[38] The Andersen thermostat is well known to affect transport properties in molecular simulations. To minimize this impact in the present studies, this thermostat is applied to atoms making up the crystalline wall only (see Figure 3.1).

The Bersenden thermostat[37] couples all the thermostated atoms to an external heat bath via a relatively crude velocity rescaling. This has the advantage of reducing large fluctuations in temperature and is a compu-

tationally efficient method to quickly adjust the temperature of the thermostated atoms.

Taking the Bersenden thermostat target temperature to be T_o and the instantaneous temperature of the thermostated atoms is T, then this velocity rescaling satisfies the global constraint that the change in temperature per time step Δt is $(T_o - T)\Delta t/\tau$. This is accomplished by scaling the velocity of every thermostated atom by λ such that $v \rightarrow \lambda v$ with

$$\lambda = \left[1 + \frac{\Delta t}{\tau}\left(\frac{T_o}{T} - 1\right)\right]^{1/2}, \tag{3.9}$$

and τ being the adjustable time constant of the thermostat. The primary advantage of the Bersenden rescaling is that it minimizes the local impact of the thermostat by minimizing

$$\sum_{i}^{N} m_i(\Delta v_i)^2,$$

the change in energy of the N thermostated atoms, due to the velocity perturbation Δv from the thermostat while preserving the Maxwellian shape of the velocity distribution in the thermostated sample.[37]

The Bersenden thermostat, as has been shown by numerical experiments of water molecules, does provide essentially identical power spectra of potential energy fluctuations and diffusivity of molecules[42] between simulations with no thermostat and simulations with thermostats of $\tau > 100\Delta t$.[42] This thermostat was only applied at small strength to the long time spreading simulation of Chapter 5, while used only to initially establish domain temperature for the capillary wave simulations (Chapter 4). For the spreading drop, $\tau = 200\Delta t$, which is at a small enough level to avoid any effects of the thermostat upon potential energy fluctuations and diffusivity[42] which implies our velocity scaling should have minimal effect of bulk molecular behavior.

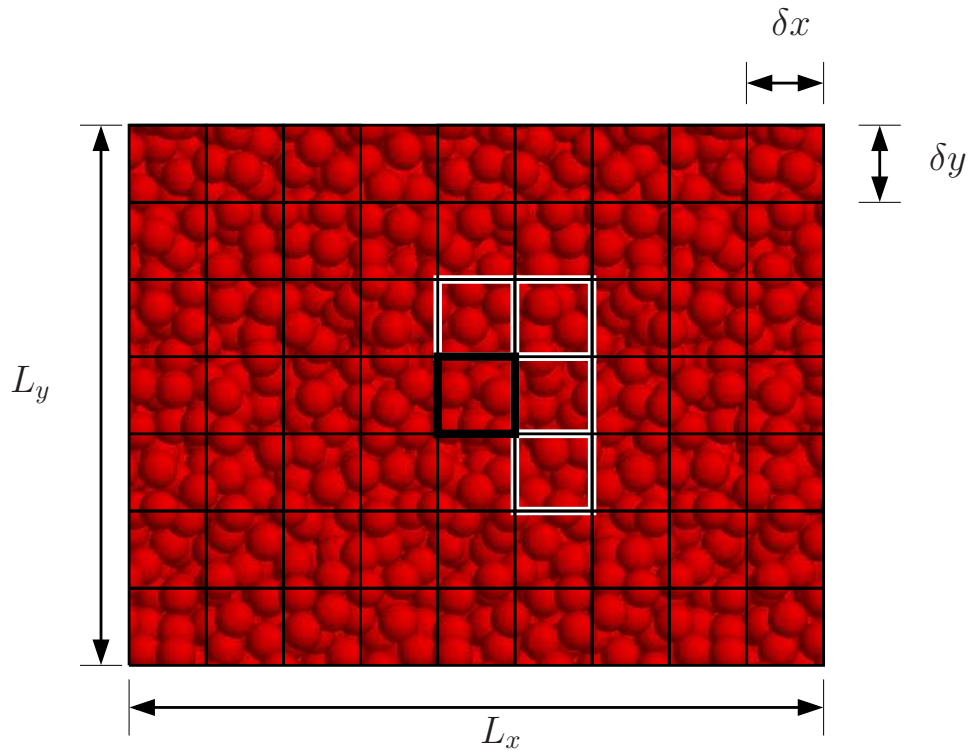

Figure 3.4: Diagram of neighbor-list calculation and implementation in $O(n)$ force calculation. L_x and L_y are the dimensions of the computational domain while δx and δy are the size of the binning in the horizontal and vertical directions, respectively.

3.2.3 Optimized Algorithms for Force Calculation

In order to bridge the time and spatial gap between molecular dynamics and continuum fluid mechanics, the drop of Chapter 5 and the flat films of Chapter 4 required around 10^5 atoms and 10^8 time steps. Because the majority of the computational cost in molecular dynamics simulation is the evaluation of the inter-atomic force,[43] a highly optimized force evaluation method is required to make such simulations tractable.

The cost of evaluating the Lennard–Jones potential (3.1) directly, without any modification in an aperiodic domain scales as the number of particles N^2, which is prohibitive for the size of simulations used in our studies. Furthermore, the simulations we employ are periodic, which without any modification of (3.1) actually have an infinite cost. However, there exist approximations of the Lennard–Jones potential that have finite cost and better computational scaling, namely the Ewald sum[44] which scales as $N^{3/2}$ and particle-mesh methods,[44] which scale as $N \log N$.

However it is not always necessary to bear the extra computational burden of an untruncated potential. Rather, by truncating (3.1) such that

$$u_{LJ}(r) = \begin{cases} 4\varepsilon \left[\frac{\sigma^6}{r^6} - \frac{\sigma^{12}}{r^{12}} \right] & r \leq r_c \\ 0 & r > r_c \end{cases}, \tag{3.10}$$

at cut-off radius r_c, molecular simulations of fluids capture many key features in the physics of fluid flow. The continuum parameter of interest that is most influenced by the presence of a truncation length is surface tension,[12,45,46] which is decreased when truncation is imposed. The benefit of truncating the potential (3.10) is that the computational cost of a molecular simulation will scale linearly with the number of atoms simulated.

Our simulations employ two efficient algorithms when evaluating (3.10), namely link-cell binning and neighbor-lists. Link-cell binning divides the domain into bins, with the size of each bin fixed. In an order N operation, the bin each atom is in can be identified and a list of all the atoms in each respective simulation bin is compiled. Shown in Figure 3.4, is a schematic of the binning procedure used in linked-cell binning, where

the black lines represent the borders of individual bins. The size of dx is

$$\delta x = \frac{L_x}{INT\left[L_x/(r_c f)\right]}, \tag{3.11}$$

where $f > 1$ is a buffer factor that allows atoms slightly farther than r_c away to be listed for use in force calculations and INT is the integer operator that removes the decimal value of any real number reducing it to an integer. A similar procedure can be applied to calculate δy. Figure 3.4 demonstrates this in two dimensions. Generalization to three dimensions is straightforward.

Using the cell lists, one can construct a neighbor-list for all atoms of the simulation. The neighbor-list is a list that contains all the close neighbors of each atom in the simulation. This list is efficiently constructed by first selecting an atom i among the atoms in a particular bin (outlined with a thick black line in Figure 3.4). Then the distance r_{ij} between atom i and every atom $j > i$ in that bin is checked to determine if

$$|r_{ij}| \leq r_c * f \qquad j = (i+1, i+2, ..., n_{\text{bin}}),$$

where n_{bin} is the number of atoms in the bin with particle i.

After constructing a list with all the interactions of particle i with the other particles in i's bin, the interactions between i and *all* the particles in *half* the surrounding bins (highlighted with bold white outlines in Figure 3.4), are checked to determine if

$$|r_{ij}| \leq r_c * f \qquad j = (1, 2, ..., n_{\text{nbin}}) \tag{3.12}$$

while n_{nbin} is the number of atoms in the neighbor bin that is being searched. By building neighbor-lists containing atoms slightly farther away than r_c, the neighbor-list can be used for several consecutive time steps before a new neighbor-list needs to be constructed, which we set at 10 time steps for all simulations.

This procedure is then repeated for all the atoms in each bin of the simulation domain. Although only half of the atoms interactions are checked (the ij interactions), because of the symmetry of Newton's third

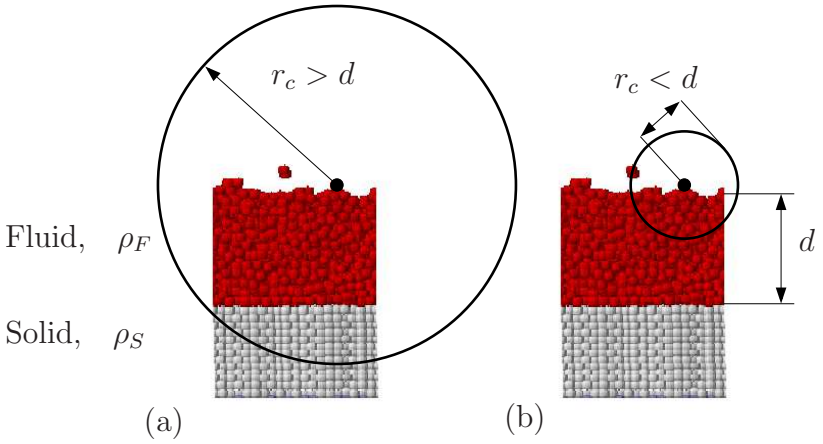

Figure 3.5: The interface of a fluid film can only interact with the solid substrate if the cut-off radius r_c is larger than the minimum thickness of the film. Thus as shown in (a), where $r_c > d$, this film will be influenced by the solid substrate. In (b), where $r_c < d$, this film will not be influence by the solid substrate, and the disjoining pressure can be neglected in modeling of this system.

law

$$f_{ij} = -f_{ji}, \qquad i, j \in (1, N) \tag{3.13}$$

with f_{ij} the force atom i exerts on atom j, and N the number of atoms in the simulation, the other half of interactions (the ji interactions) are easily included into the force calculation.

3.2.4 Disjoining Pressure and Cut-off Radius

In addition to the Laplace pressure supplied by the surface energy and curvature of the interface, thin liquid films (thicknesses less than 100 nm[47]) are influenced by a non-local interaction between the fluid film and the solid substrate that supports it. This interaction is known as the disjoining pressure. Israelachvili[48] modeled this interaction by assuming a fluid film of thickness d composed of fluid atoms with a number density of ρ_f, sits atop an infinite half space of solid atoms with a number density of ρ_s, where all atoms interact via a dispersion $(1/r^6)$ attraction. This leads to

an energy of interaction that is a function of film thickness,

$$\phi(h) = -\frac{A}{12\pi d^2}, \tag{3.14}$$

where A is the Hamaker's constant, with

$$A = 4\pi^2 \varepsilon_{sf} \rho_s \rho_f, \tag{3.15}$$

and ε_{sf} the Lennard–Jones energy parameter. Despite its presence in physical systems, disjoining pressure is not a factor in atomistic simulations for films thicker than the cutoff radii. If the cut-off radius is smaller than the thickness of a film locally, as shown in Figure 3.5, then there is no interaction between the fluid interface and the solid substrate and correspondingly no disjoining pressure. All simulations employed in this work had film thicknesses greater than r_c, thus when calculating the pressure on an interface in the corresponding continuum model, no disjoining pressure needed to be included.

3.2.5 Polymer Neighbor List

In addition to efficiently identifying interactions of the truncated Lennard–Jones force, there must also be an efficient manner to determine the atoms that interact via the FENE potential (3.2). Each atom of the simulation is given a polymer identification number n_{id} such that

$$INT[n_{id}/N_p] = p_{id}, \tag{3.16}$$

with N_p being the length of the fluid polymers, and p_{id} identifies the polymer in which each fluid atom is contained. The position of any atom on a particular polymer chain is identified by

$$n_p = MOD(n_{id}, N_p), \tag{3.17}$$

n_p being the local position of an atom in the polymer chain, and MOD is the modulus operator. Assuming that the polymer reference length $R_o \leq r_c$, then when building the neighbor-list, it is simple to determine if two atoms interact with the FENE potential by first determining if two atoms

are on the same polymer (p_{id}) and then if their polymer positions n_p differ by 1. This identification of adjacent atoms in a polymer chain is stored as a logical variable within the neighbor-list discussed in Section 3.2.3. This logical variable is either "true" or "false", depending on whether an interaction includes the FENE potential, and only if this variable is true will the FENE force be included in an inter-atomic force.

3.2.6 Parallelization

The simulations required for both the spreading droplet (Chapter 5) and the relaxation of thermal capillary waves (Chapter 4) consisted of domains containing several hundred thousand atoms and required hundreds of million time steps. Such computations would require years on a single processor machines. The algorithm was therefore implemented in parallel.

The computational domains we consider are approximately one dimensional: they are long in the x-direction (up to 1760σ) with narrow widths in z (6σ) and little gas phase, with fluid films usually less than 1/3 the height of the simulation domain. These simulation characteristics suggest a one-dimensional domain decomposition across processors.

We followed the parallel algorithms developed by Plimpton[43] for parallel short-range molecular dynamic simulations. By decomposing our domain in one dimension, into P sub-domains of arbitrary length, the force calculation and integration of the atoms in those sub-domains can be geometrically distributed over P processors. This domain decomposition is both intuitive and also has been shown to scale efficiently for a large range of simulation sizes and processor numbers.[43]

This domain decomposition can easily be included into the already efficient neighbor-list and linked-cell binning techniques used to optimize the force calculation in a serial molecular dynamics simulations. However, instead of the periodic boundary conditions used on each domain in serial, the subdomain's boundary conditions were determined by the atoms from the adjacent sub-domains, as shown in Figure 3.6 (a) and (b). Atoms from other processors that are contained in the boundary bins of the neighbor domains are stored as ghost atoms locally. These atom's positions are up-

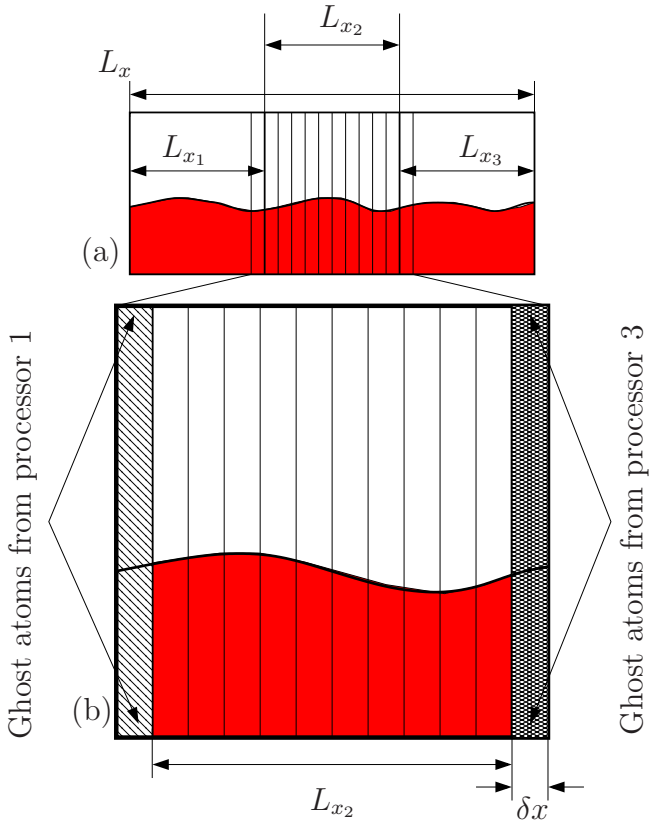

Figure 3.6: (a) Diagram of domain decomposition across 3 processors, with sub-domain lengths such that $L_x = L_{x_1} + L_{x_2} + L_{x_3}$. Vertical lines indicate the boundaries of the bins used to compute linked-lists as explained in Section 3.2.3. (b) Zoomed view of subdomain on processor 2. The size of the ghost region of each domain is identical to the binning used in creating the linked-lists.

dated every time step, so that the force interactions across processors' domains are still computed locally. Furthermore, every time a new neighbor-list is created, the atoms that move across processors boundaries are moved over to that processor and stored locally.

Having built a neighbor-list that can be reused for several integration time steps, as discussed in Section 3.2.3, the only information that needs to be updated between processors every time step is the location of the ghost particles so that they can be used for force calculations. The local calculation of all interactions across domain boundaries leads to some redundant calculation of the forces between ghost particles and particles actually on each processor. Despite the redundancy of boundary atom force calculations, the current, truncated Lennard–Jones simulation scales particularly well with P, the number of processors (see Figure 3.7). The computational cost of rearranging atom lists and redundant computation of ghost particle forces is negligible until average domain lengths are less than ten cutoff radii long. The spreading simulation of Chapter 5 was run on 64 processors at either Lonestar or Ranger of the Texas Advanced Computing Center. Because of the nature of the spreading, domain decomposition was dynamic, however by inspection the initial distribution of processors and all subsequent distributions did not become thinner than ten cutoff radii. Because of the static nature of the stable films in the capillary wave study of Chapter 4, the domain decomposition was also static throughout the run of the simulation. Capillary wave studies used as many as 24 processors, with no single processors domain less than ten cutoff radii in length.

For the flat, stable films of the thermal capillary wave study of Chapter 4, the geometric decomposition of the domain yields a nearly uniform distribution of the atoms across the processors. The computational load is well balanced since every processor has almost the same amount of work to do. However the uniform geometric distribution of Chapter 4 would not evenly distribute atoms in the spreading drop. What is more, as the drop spreads, the optimal processor distribution changes. Therefore we developed an adaptive load balancing approach. In order to approach an optimal decomposition, the boundaries of the sub-domains between processors should migrate to balance the workload evenly across processors. "Workload" on a processor is well approximated by the size of the local neigh-

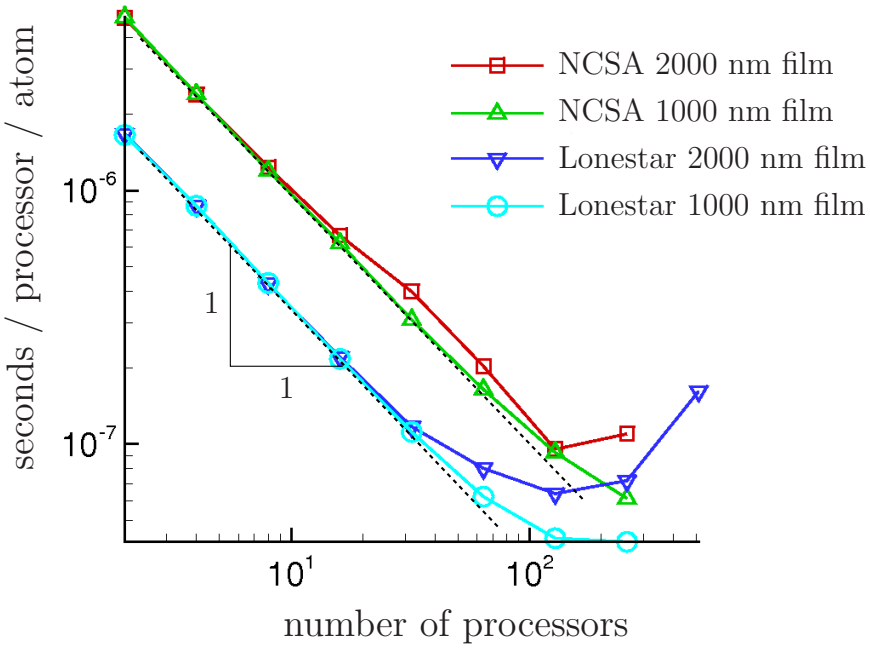

Figure 3.7: Scaling data for simulation tested at two TeraGrid sites. Simulations were timed for five consecutive sets of 20 time steps. These times were averaged and divided by number of particles. The code was tested on 2, 4, 8, 16, 32, 64, 128, 256, and 512 processors. The super-imposed dashed lines are of slope negative one, which is the idealized scaling.

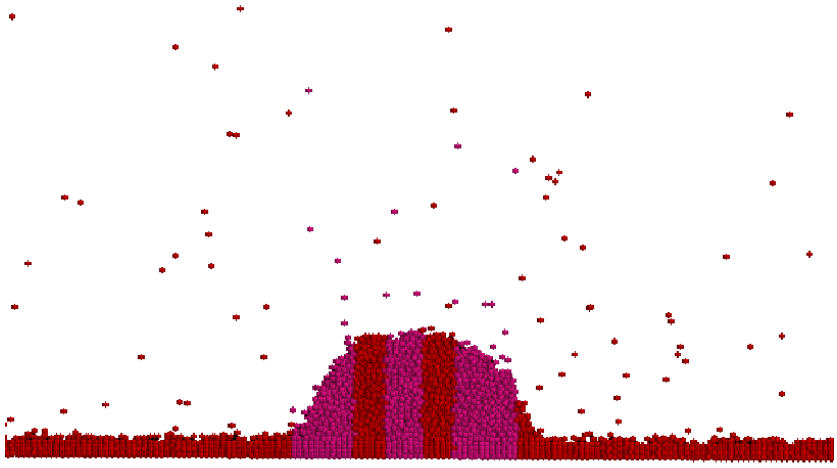

Figure 3.8: Snapshot of the dynamic boundaries of processors. This domain was originally evenly divided among processors, and over the process of 10,000 time steps, the load was evenly balanced. Each alternating color is one of seven processors. The domain of a particular processor can become almost as thin as one truncation length.

bor list, since this is approximately the number of force calculations. Before computing a new neighbor-list, the size of old neighbor-lists are compared between adjacent processors, and if the neighbor-list of one processor is 10% larger than its neighbor, the boundary is shifted by $L_x/100$ in the direction towards the processor with the greatest work load. The new boundaries are then applied in the same manner as when boundaries are checked for atoms that diffused out of the domain, and atoms that are no longer contained within a processor's boundaries are moved appropriately. Throughout the simulation this procedure is carried out every time neighbor lists are created, which leads to an optimized domain decomposition that adapts to the bulk atomic flow, as shown in Figure 3.8. In the large spreading simulation of the droplet of Chapter 5, the drop spreads over the span of 10^8 time steps while neighbor lists are updated every 10 time steps, so the redistribution of load easily tracks the spreading of the drop with the parameters selected.

3.3 Continuum Modeling

The testing of molecular fluid behavior against continuum fluid predictions requires continuum properties be assigned to the molecular fluids. The simulated polymers used in the spreading drop (Chapter 5) and thermal capillary waves (Chapter 4) do not model any particular real fluid with published continuum fluid properties. Rather, these properties must be measured directly from the molecular fluids, which is best done in separate fluid simulations. In order to determine both the bulk Newtonian viscosity and the heat conductivity of a molecular fluid, Green-Kubo integrals were used, as discussed in Section 3.3.1. Section 3.3.2, discusses the surface tension of a molecular fluid, measured via the spatial integration of the pressure tensor of a suspended fluid film. The evaporative model of the stochastically driven, evaporating drop (Chapter 5) required a value of the latent heat of vaporization. Section 3.3.3 discusses the use of numerical experiments to determine a value for the critical temperature and pressure of the molecular fluid for use in a semi-empirical model of latent heat of vaporization.[49] Finally, in order to compare the linearized predictions of thermal capillary wave dynamics to the dynamics of a molecular fluid-vapor interface, as will be done in Chapter 4, the height-height time correlations predictions of Section 2.2, will be compared with measurements of height-height correlations in the molecular fluids. The numerical methods of calculating such correlations from molecular simulation data are addressed in Section 3.3.4.

3.3.1 Green-Kubo: Viscosity, Thermal Conductivity

To compare with continuum models, we need the viscosity and thermal conductivity properties. Theses values are not fully documented for FENE Lennard–Jones polymers, and therefore need to be computed. We did this using Green-Kubo formulations, which relate continuum transport coefficients to integrals of time correlations[50,51] of molecular systems.

The shear viscosity η of a Newtonian fluid, as demonstrated by

Zwanzig[52] can be calculated by evaluating

$$\eta = \frac{V}{k_B T} \int_0^\infty \langle \tau_{xy}(t) \tau_{xy}(0) \rangle \mathrm{d}t, \tag{3.18}$$

with τ_{xy} the virial stress, and V and T the volume and temperature of the sample, respectively. The virial stress as was originally constructed by Irving and Kirkwood[53] and calculates the Cauchy stress of a volume of particles Ω by a sum over all the particles i in that volume. The sum involves both the momentum flux in and out of the volume and the moments via external and internal forces such that

$$\tau_{\alpha\beta} = \frac{1}{\Omega} \sum_{i \in \Omega} \left(\underbrace{m_i v_\alpha^i v_\beta^i}_{\text{momentum}} + \underbrace{\frac{1}{2} \sum_{j=1}^{N} r_\alpha^{ij} f_\beta^{ij}}_{\text{forces}} \right), \tag{3.19}$$

and α and β are the component induces of vectors and tensors. r_α^{ij} is the α component of the vector

$$\mathbf{r}_{ij} = \mathbf{r}_i - \mathbf{r}_j, \tag{3.20}$$

with $\mathbf{r}_i$ and $\mathbf{r}_j$ the positions of particles i and j, respectively. The term f_β^{ij} is the β component of the force vector of interaction between particle i and j.

The thermal conductivity λ of molecular systems can be calculated in a similar manner,[39,54]

$$\lambda = \frac{V}{3 k_B T^2} \int_0^\infty \langle \mathbf{J}_Q(t) \cdot \mathbf{J}_Q(0) \rangle \mathrm{d}t, \tag{3.21}$$

where $\mathbf{J}_Q$ the heat flux vector

$$\mathbf{J} = \frac{1}{V} \sum_{j=1}^{N} \left(e_j \mathbf{v_j} + \frac{1}{2} \sum_{i=1}^{N} \mathbf{r}_{ij} (\mathbf{f}_{ij} \cdot \mathbf{v}_j) \right), \tag{3.22}$$

and

$$e_j = \underbrace{\frac{1}{2} m v_j^2}_{\text{kinetic}} + \underbrace{\frac{1}{2} \sum_{k=1}^{N} u(r_{kj})}_{\text{potential}} - \langle e \rangle. \tag{3.23}$$

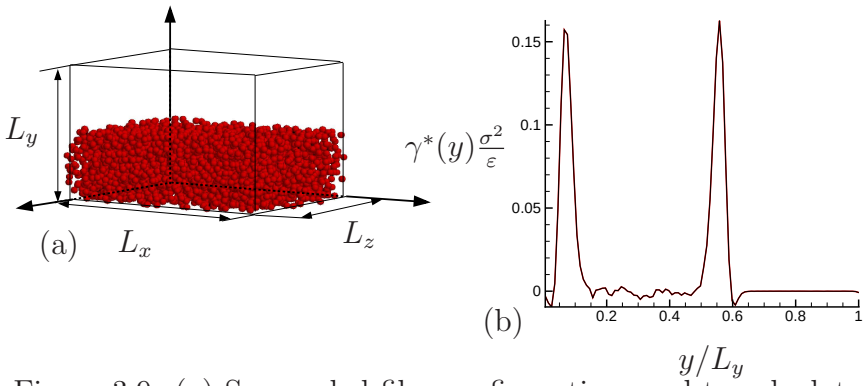

Figure 3.9: (a) Suspended film configuration used to calculate surface tension. The domain is periodic with lengths L_x,L_y,L_z. The $x - z$ plane is tangential, while the y axis is normal to the fluid interface. The difference between the normal and tangential pressure as a function of y is calculated and then integrated to yield surface tension measurements via (3.24). (b) Shown are sample values of $\tau_{yy}(y) - 1/2(\tau_{xx}(y) + \tau_{zz}(y))$ a two atom polymer at $Tk_B = 0.84\varepsilon$.

The term e_j is the difference in the total energy of particle j from that of the average of all the particles energies, $\langle e \rangle$. The energy of particle j is a summation of both the kinetic energy as well as the sum of the pairwise interaction of particle j and all other atoms in the system. In order to calculate the viscosity and thermal conductivity of individual fluids, small periodic simulations measuring 1000 nm^3 of bulk fluid (with approximately 10^4 fluid atoms) were simulated. Green-Kubo averages were calculated for 10^7 time steps for each fluid. Correlation data was computed via the methods discussed in Section 3.3.4 in order to arrive at values for both η and λ via, (3.18) and (3.21), respectively.

3.3.2 Surface Tension

The dynamics of fluid films are often driven by the pressure supplied by surface tension and interface curvature. The surface tension of some of the fluids we consider have not been reported before. Thus, in order to study thin film dynamics of several different fluid films, the surface tension also needs to be computed. In order to evaluate surface tension, a suspended fluid film is simulated with periodic boundaries, as shown in Figure 3.9(a). Surface tension of a molecular fluid is defined as the integral through the

fluid interface of the averaged difference across the interface of the normal and tangential stress γ^*,[46,55]

$$\gamma = \frac{1}{2}\int_0^L \gamma^*(y)\mathrm{d}y, \tag{3.24}$$

where

$$\gamma^*(y) \equiv \left\langle \tau_{yy}(y) - \frac{\tau_{xx}(y)+\tau_{zz}(y)}{2} \right\rangle, \tag{3.25}$$

Here $\tau_{\alpha\beta}$ is the virial stress tensor (3.19). The factor of $1/2$ accounts for the two interfaces. Shown in Figure 3.9(b) is a typical plot of the difference between the tangential and normal pressures, $\gamma^*(y)$, which is the quantity integrated to yield surface tension values.

3.3.3 Latent Heat of Vaporization

The evaporation dynamics used to capture the effect of evaporation in the spreading drop (Chapter 5) requires a value for the latent heat of evaporation $\mathcal{L}$. This can be approximated by the latent heat of vaporization of argon if a single-atom Lennard–Jones fluid is simulated.[11] However, because the spreading droplet required a Lennard–Jones polymer, which is not a specific model of any particular fluid, such a direct connection to measured latent heats of vaporization does not exist. Semi-empirical models have been shown to predict the latent heat of vaporization for a wide range of fluids,[49]

$$\mathcal{L} = \frac{4.35T_c(1.0-P_r)^{0.69}\log P_r}{1-1/T_r}, \tag{3.26}$$

with T_r the vapor temperature of the fluid non-dimensionalized by the critical temperature T_c, and P_r is the vapor pressure of the fluid scaled by the critical pressure. Thus we can estimate $\mathcal{L}$ from T_c and P_r. These are estimated in auxiliary simulations, shown in Figure 3.10(a). A periodic box is filled with the fluid molecules of interest. The fluid is atop a wetting crystal and the volume of the box is held constant. The thermostating and integration methods are the same as used for the other molecular simulations of this work, namely velocity-Vertlet integration (see Section 3.2.1) and an Andersen thermostat on substrate atoms only (see Section 3.2.2). One hundred simulations with increasing temperature, but otherwise identical yield

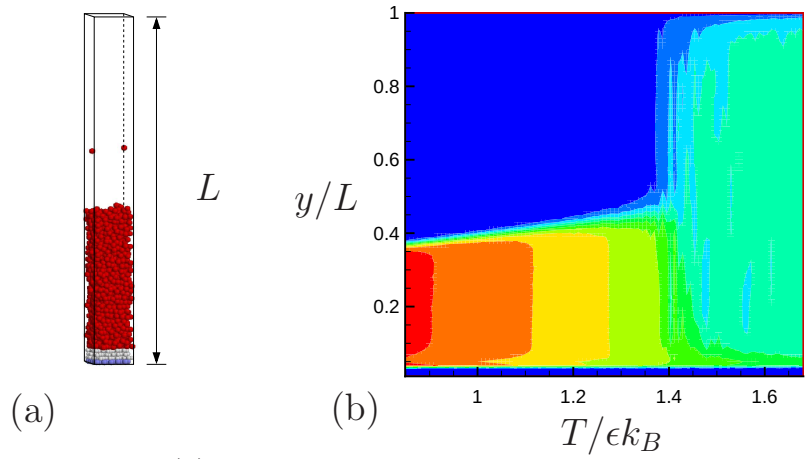

Figure 3.10: (a) Periodic simulation of a fluid sample used for each temperature T. (b) Density plots of each domain as a function of vertical position (y/L) and temperature T, measured after each simulation has equilibrated. Blue regions indicate low number densities, while red regions indicate high number densities, ranging from 0 to $0.81/\sigma^3$.

the density data, shown in Figure 3.10(b). The average density in the vertical dimension is plotted for each averaged bin as a function of simulation temperature. The critical point of the fluid is the temperature (and corresponding pressure) when there is no discernible fluid-vapor interface, which can be seen as the point when the density of fluid atoms suddenly become homogeneous across the entire domain. For the two-atom polymer, used in the spreading drop, this is approximately $T_c = 1.44\epsilon k_B$ (170K) in Figure 3.10(b).

The spreading drop was simulated at a temperature of $T/T_c = 0.58$, discussed in Chapter 5, and a pressure of $P/P_c = 0.003$, which yields a predicted latent heat of vaporization (assuming Lennard–Jones pair parameter corresponding to argon) of 649.17 kJ/kg. This value of $\mathcal{L}$, when included into the evaporating-stochastic lubrication equation (2.87) used to model the spreading droplet (Figure 5.2), appears to reproduce the homogeneous condensation of fluid at the edges of the domain, where evaporation and condensation are the only mechanisms for fluid accumulation. This apparent agreement between the model and the molecular fluid further supports that the value of $\mathcal{L}$ calculated here via (3.26) is sufficiently accurate.

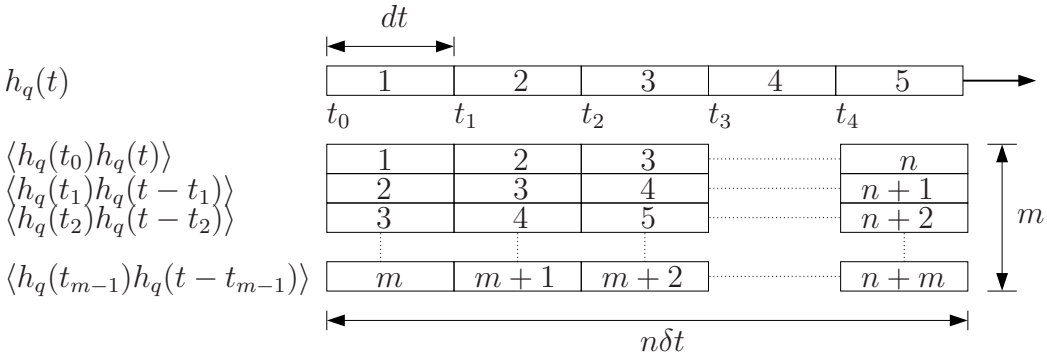

Figure 3.11: Diagram of approximating correlation function $\langle h_q(0)h_q(t)\rangle$, when given single time evolution data $h_q(t)$. The evolution data is presented as the horizontal strips with the numbering used to label different regions of time evolution. The data of $h_q(t)$ being used for the multiple correlations being calculated simultaneously is reflected by the numbers in the middle of the horizontal strips associated with the correlations $\langle h_q(t_{m-1})h_q(t-t_{m-1})\rangle$.

3.3.4 Correlations

The continuum model of height-height time correlations, as derived in Section 2.2, predicts exponential decays with initial amplitudes and decay rates as functions of wavenumber. In order to test the continuum predictions of the height-height correlations of the Fourier modes of thermal capillary waves, which are predicted to be exponential decays, statistically averaged values of $\langle h_q(0)h_q(t)\rangle$ were fit to exponential decays of the form

$$\langle h_q(0)h_q(t)\rangle = Ae^{-Bt}, \tag{3.27}$$

where A and B are two independent variables, corresponding to the mean-squared amplitude and decay rate, respectively.

The averaged values of the height-height correlation can be computed using established techniques, which are documented in detail by Rapaport.[39] As shown in Figure 3.11, the time evolution of the variable $h_q(t)$ is collected, represented by a contiguous series of shorter intervals of δt, labeled ("1", "2", "3",...). Given that the time t_0 is arbitrary in the evolution of an interface fluctuating around equilibrium, multiple correlations with different initial times can be gathered and eventually averaged together to approximate $\langle h_q(t_0)h_q(t)\rangle$. Thus rather than measuring corre-

lations one at a time, m separate correlations can be measured simultaneously. Furthermore, assuming that $B > 0$, the correlations eventually decay in time, thus correlation measurements need only be measured for finite periods. The number of δt intervals can be limited to n, assuming $Bn\delta t \ll 1$. After a measurement time of $n\delta t$, correlation data can be averaged into the other collected correlations and a new correlation measurement can begin.

Having estimated the time evolution of $\langle h_q(t)h_q(0)\rangle$, the values of A and B can be approximated by using a least-of-squares fit to the correlation data. We used least of squares to minimizes the mean squared distance between the measured correlation values and equations of the form (3.27). The fitting of A and B is accomplished by creating a cost function W, which is then minimized by solving for A and B, with the two constraints

$$\frac{\partial W}{\partial A} = \frac{\partial W}{\partial B} = 0. \tag{3.28}$$

We initially defined W as

$$W = \sum_{i=0}^{N} \left[\log(\langle h_q(0)h_q(t_i)\rangle) - \log(A) + Bt_i\right]^2. \tag{3.29}$$

where N is the number of discrete samples used to build $\langle h_q(0)h_q(t)\rangle$ and $t_i = \delta t(i-1)$ and δt is the time between data points of the correlation data. However, when inspecting the correlation data of interface profiles from molecular dynamics simulations, the initial correlation fits were deemed to be influenced by the long-time decaying tail of the correlation. In order to focus on the initial decay behavior we modified the cost function such that,

$$W = \sum_{i=1}^{N} e^{-B_{\text{guess}}t} \left[\log(\langle h_q(0)h_q(t_i)\rangle) - \log(A) + Bt_i\right]^2. \tag{3.30}$$

The value B_{guess} is the guess at the correlation decay rate before a new value of B is calculated. Once the new value of B is calculated via (3.28), B_{guess} is replace by B and B is recalculated. This process is then iterated five times. The calculated values of amplitudes A and decay rates B as a function of wavenumber q were indistinguishable after three, five and eight iterations. Thus our iteration procedure does not alter any of the conclusions of this work. As will be seen in Figure 4.2, this approach provides ap-

parently excellent fits to the decorrelating amplitudes of thermal capillary waves for the range of wavenumbers analyzed.

3.4 Numerical Solutions of the Thin-Film Equations

In order to make direct comparisons between molecular simulations and continuum models in Chapter 5, solutions of the continuum model are needed, which entails solutions to fourth-order and nonlinear equations. Its complexity precluded an analytic solution, thus we solved the equations numerically. We used implicit schemes in order to avoid costly time step restrictions of explicit methods with fourth-order derivatives in space. The spatial discretization was via Fourier collocation derivative operators, which is discussed in Section 3.4.1. Section 3.4.2 discusses our time integration, namely a Crank-Nicholson integration scheme, which included the random forcing term of the stochastic evaporating lubrication equation (2.87).

3.4.1 Fourier Collocation Solver

In order to calculate the derivatives of the interface profile $h(x)$, the interface is discretized such that numerical solutions of the interface profile are denoted as the vector $\mathbf{h}$ and composed of elements

$$h_j \in \mathbf{h}, \qquad j \in 0, 1, 2, ..., N-1, \tag{3.31}$$

such that $h(x_j) = h_j$ at N equally spaced grid points at positions

$$x_j = 2\pi j/N, \qquad j \in 0, 1, 2, ..., N-1. \tag{3.32}$$

Thus the height of the interface at position x_j can be referenced as h_j, which can be decomposed into its discrete Fourier components $\hat{h}_k$ as

$$\hat{h}_k = \frac{1}{N} \sum_{j=0}^{N-1} h_j e^{-ikx_j}. \tag{3.33}$$

The corresponding inverse transform is

$$h_j = \sum_{k=-N/2}^{N/2-1} \hat{h}_k e^{ikx_j}. \tag{3.34}$$

The derivative of $\mathbf{h}$ at position x_j is thus approximated as

$$\frac{dh_j}{dx} = \sum_{k=-N/2+1}^{N/2-1} ik\hat{h}_k e^{ikx_j}. \tag{3.35}$$

By substituting (3.33) into (3.35), the derivative of h_l can be simplified to

$$\frac{dh_l}{dx} = \frac{1}{N} \sum_{k=-N/2+1}^{N/2-1} \sum_{j=0}^{N-1} ikh_j e^{\frac{2\pi ik}{N}(l-j)}, \qquad l = 0, 1, 2, ..., N-1. \tag{3.36}$$

A derivative operator $\mathbf{D}$ is thus constructed as a $N \times N$ matrix with elements d_{lj}, such that

$$\frac{d\mathbf{h}}{dx} = \mathbf{Dh}, \tag{3.37}$$

and

$$d_{lj} = \frac{1}{N} \sum_{-N/2+1}^{N/2-1} ike^{\frac{2\pi ik}{N}(l-j)}, \qquad l = 0, 1, 2, ..., N-1. \tag{3.38}$$

The expression for d_{lj} can be simplified, as is demonstrated by Moin[56] to

$$d_{lj} = \begin{cases} \frac{1}{2}(-1)^{l-j} \cot\left[\frac{\pi(l-j)}{N}\right], & \text{if } l \neq j \\ 0, & \text{if } l = j. \end{cases} \tag{3.39}$$

3.4.2 Crank-Nicholson Integration

The time integration of the evaporating stochastic lubrication equation, (2.87) is via the implicit Crank–Nicholson method. This method discretizes time into time steps of Δt, such that

$$t_n = n\Delta t. \tag{3.40}$$

We define $\mathbf{h}^n$ as the interface at time t_n. We present the algorithm for a generic coupled ordinary differential equation

$$\frac{d\mathbf{h}^n}{\mathrm{d}t} = \mathbf{F}(\mathbf{h}^n, \xi^n), \tag{3.41}$$

where $\mathbf{F}$ is the differential operator of the ODE and is a function of a normalized random noise ξ^n at time step n, which is composed of elements

$$\xi_j^n \in \xi^n, \qquad j \in 0, 1, 2, ..., N-1, \tag{3.42}$$

each of which has the statistical properties

$$\langle \xi_j^n \rangle = 0, \qquad \text{and} \qquad \langle \xi_j^n \xi_k^m \rangle = \delta_{jk}\delta_{mn}. \tag{3.43}$$

The Crank-Nicholson scheme approximates (3.41) by

$$\frac{\mathbf{h}^{n+1} - \mathbf{h}^n}{\Delta t} = \frac{1}{2}\left(\mathbf{F}(\mathbf{h}^{n+1}, \xi^{n+1}) + \mathbf{F}(\mathbf{h}^n, \xi^n)\right), \tag{3.44}$$

which upon application of the approximation

$$\mathbf{F}(\mathbf{h}^{n+1}, \xi^{n+1}) \approx \mathbf{F}(\mathbf{h}^n, \xi^{n+1}) + \frac{\partial \mathbf{F}(\mathbf{h}^n, \xi^{n+1})}{\partial \mathbf{h}}\delta\mathbf{h} \tag{3.45}$$

where ξ^{n+1} is the "future" noise term, yields

$$\delta\mathbf{h} = \left(\mathbf{I} - \frac{\partial \mathbf{F}(\mathbf{h}^n, \xi^{n+1})}{\partial \mathbf{h}}\right)^{-1} \left(\frac{1}{2}\mathbf{F}(\mathbf{h}^n, \xi^{n+1}) + \frac{1}{2}\mathbf{F}(\mathbf{h}^n, \xi^n)\right)\Delta t \tag{3.46}$$

where $\mathbf{I}$ is the identity matrix. $\mathbf{h}^{n+1}$ is found by iteratively solving (3.46) for $\delta\mathbf{h}$, until the residual

$$R = \frac{\left|\frac{\mathbf{h}^{n+1}-\mathbf{h}^n}{\Delta t} - \frac{1}{2}\left(\mathbf{F}(\mathbf{h}^{n+1}, \xi^{n+1}) + \mathbf{F}(\mathbf{h}^n, \xi^n)\right)\right|}{|\mathbf{h}^n|}, \tag{3.47}$$

is less than 10^{-6}, where $|...|$ is the vector magnitude operator. This construction is similar to a non-stochastic solver, however the right hand side of the ODE includes a stochastic stress term of ξ^n and ξ^{n+1}, which are both known and can be included into $\mathbf{F}$. Implementation of the iterative scheme involves the analytic differentiation of $\frac{\partial \mathbf{F}(\mathbf{h},\xi)}{\partial \mathbf{h}}$, which is a matrix of

elements

$$\frac{\partial F_i(\mathbf{h},\xi)}{\partial h_j} \in \frac{\partial \mathbf{F}(\mathbf{h},\xi)}{\partial \mathbf{h}} \quad \text{for} \quad i,j = 0,1,...,N-1, \tag{3.48}$$

where $F_i(\mathbf{h},\xi)$ is the ith element of the vector $\mathbf{F}(\mathbf{h},\xi)$, and $i = 0,1,...,N-1$.

Chapter 4

Thermal Capillary Waves

In the present study,[57] we use idealized but realistic atomistic simulations to provide simple-fluid data for directly assessing the breakdown of the continuum description for the decay of thermal capillary waves. Results are compared to the solutions of the viscous flow equations for the relaxation of thermal capillary waves, *e.g.* Henle *et al.*,[22] discussed in Section 2.2. Section 4.1 describes briefly our model system including the numerical methods used to simulate it. More complete details of the molecular simulations can be found in Section 3.2. The results of the simulations are presented in Section 4.2 and further discussed in Section 4.3.

4.1 Atomistic Simulation of Model Fluid Films

The atomic interactions in the fluid are modeled with the Lennard–Jones pair potential, which includes a simple $1/r^6$ dispersion (van der Waals) attraction and an empirical $1/r^{12}$ repulsion:

$$u_{LJ}(r) = \begin{cases} 4\varepsilon \left[\frac{\sigma^6}{r^6} - \frac{\sigma^{12}}{r^{12}} \right] & r \le r_c \\ 0 & r > r_c \end{cases}, \tag{4.1}$$

where ε is the interaction energy, r is the distance between the two atoms, and σ is the interaction length scale (zero force is at $r = 2^{1/6}\sigma$). The simulations employ a cutoff radius $r_c = 2.5\sigma$. Most physical properties are insensitive to this r_c, but it does decrease the effective surface tension by about a factor of two.[46] The Lennard–Jones atoms are joined into poly-

mers using the Finite Extensible Nonlinear Elastic (FENE) potential[36,58]

$$u_{\mathrm{f}}(r) = \begin{cases} -\frac{1}{2}kR_o^2 \log\left[1 - \frac{r^2}{R_o^2}\right] & \text{for } r < R_o \\ \infty & \text{for } r \geq R_o \end{cases}, \tag{4.2}$$

where k is a spring strength and R_o is a bond-length parameter. Taking $k = 30\epsilon/\sigma^2$ and $R_o = 1.5\sigma$ has been shown to provide realistic packing without imposing any significant new restriction on the numerical time step.[36] In our initial set of simulations, with two-atom molecules making up the fluid the fluid, we simulated five films thicknesses: 6σ, 12σ, 24σ, 48σ, and 96σ. If Lennard–Jones parameters for argon were specified, this would correspond to films ranging from 2 nm to 32 nm thick. Each simulation domain had a length of $L = 590\sigma$ and a width of $W = 8\sigma$. Results from a $50\sigma \times 50\sigma$ simulation were used confirm that our results are independent of the simulation domain size (*e.g.* see Figure 4.8). The quasi-one-dimensional $590\sigma \times 8\sigma$ domain used provides lower wavenumber behaviors with little additional computational cost.

The solid substrate is composed of four layers of Lennard-Jones atoms frozen into an FCC lattice. The masses and interaction energies of the substrate atoms were ten times that of the fluid to insure that the wall remained solid. In order to model the stiffness of an extensive solid, the very bottom layer of substrate atoms were held fixed. The velocity-Verlet algorithm was used to advanced the equations of motion in time. This method has good but imperfect energy conservation properties, so a weak stochastic Andersen[38] thermostat (see Section 3.2.2) was applied to the substrate atoms to maintain a constant temperature through the course of the simulation. This thermostat randomly re-assigns velocities of substrate atoms, choosing the new velocity from a Boltzmann distribution, with a probability of reassignment of $p = 0.005$ each time step. By applying this thermostat just to the substrate, it is not expected to have any effect upon the thermal capillary waves of interest.

Fluid parameters were determined independently using established methods[39] with small-scale auxiliary simulations. Viscosity was computed using the Green-Kubo formulation[39] as is discussed in Section 3.3.1. Similarly, the surface tension was computed in a suspended film configuration[46]

with two free fluid-vapor interfaces as discussed in Section 3.3.2.

Analyzing the statistics and dynamics of the thermal capillary waves in the atomistic system requires a definition of the interface location based on the atom positions. We base our definition on the density fields constructed by averaging atomic positions every time step in small cubic bins. A bin volume of σ^3 was used in most calculations, but results are essentially identical for bin volume of $0.02\sigma^3$ for the wavenumbers of interest, as will be seen in Figures 4.3 and 4.4. The surface shape was defined based on atom positions averaged over $\tau_{LJ} \equiv \sqrt{\sigma m/\epsilon}$. This time scale is on the order of the molecular vibrations, and is thus much faster than the relaxation of thermal capillary waves. Averages over $2\tau_{LJ}$ (also to be seen in Figure 4.3) do not alter results. For each x and z column of bins, the data were interpolated by linear functions to define $\rho(x, y, z, t)$. From this, the interface $y = h(x, z, t)$ is defined by the $\rho(x, y, z, t) = \rho_c \equiv \rho_{\text{bulk}}/10$ isopleth (see Figure 4.1). Results are insensitive to ρ_c and the calculated decay rates and amplitudes (see Figures 4.3 and 4.4) are unchanged by values of $\rho_c = \rho_{\text{bulk}}/6$, $\rho_{\text{bulk}}/10$ and $\rho_{\text{bulk}}/16$. This discrete interface is Fourier transformed to $h_{\mathbf{q}}(t)$, and the ensemble averaged time correlations $\langle h_{\mathbf{q}}(t)h_{\mathbf{q}}(0)\rangle$ are computed and fitted to exponentials to calculate $\omega(q)$ as shown in Figure 4.2.

A consistent definition of a fluid-vapor interface is an obvious necessity for any study of the dynamics of fluid-vapor interface dynamics. Although we employ a simple cutoff-density definition, this definition is not applicable in all fluids.[59–61] The inherent density fluctuations near the fluid-vapor interface found in atomic Lennard–Jones fluids[59,60] as well as liquid gallium interfaces[61] must be included into interface definitions of any fluids that exhibit this behavior. Cutoff density based interfaces of such fluids could mistakenly ascribe the position of a local minimum in these fluctuations as the fluid-vapor interface position and lead to error in measuring interface dynamics. However, the amplitudes of these fluctuations are suggested to be a function of the fluid temperature relative to the critical temperature.[59,60] As will be shown in Section 4.3, the fact that for a wide range of fluid temperatures (relative to critical temperature), we see no change in behavior, suggests that local fluctuations in fluid density are not a characteristic of the simulated fluids.

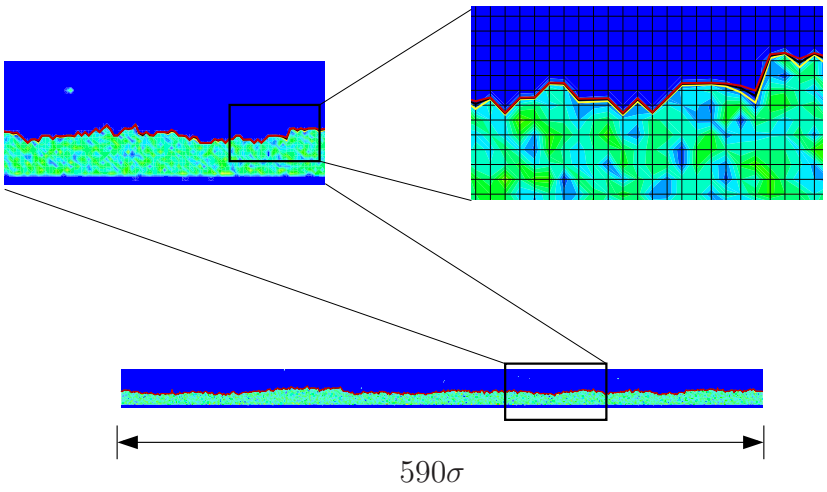

Figure 4.1: Density fields and interface location defined by the ρ_c isopleths: yellow $\rho_c = \rho_{\text{bulk}}/6$, **black** $\rho_c = \rho_{\textbf{bulk}}/10$, and red $\rho_c = \rho_{\text{bulk}}/16$. These lines are superimposed over the density σ^3 bins.

That our interface definition is independent of the numerical parameters used in the statistical accumulation is clearly demonstrated for a wide-range of wavenumbers in Figures 4.3 and 4.4. An additional discussion of these different parameters and the consistency of our interface definition is included in Section 4.3.

4.2 Results

The $\omega(q)$ of all films simulated are plotted in Figure 4.5 and compared to (2.51). According to (2.53), all of the data should collapse onto a curve $\omega \sim q^4$ for small q and a $\omega \sim q$ curve for larger q. The longer wavelengths do indeed asymptote to the $\omega \sim q^4$ line, while all of the films except the thinnest also show a $\omega \sim q$ behavior for larger q. This thinnest film is presumably too thin to be effectively thick even relative to the shortest wavelengths. Unexpectedly, the shorter wavelengths of every film also apparently has its own approximate $\omega \sim q^2$ power law, which is not anticipated by the continuum theory.

With these data scaled by the atomic scale σ, rather than film thickness d, Figure 4.6 shows collapse of the curves in the $\omega \sim q^2$ region, indica-

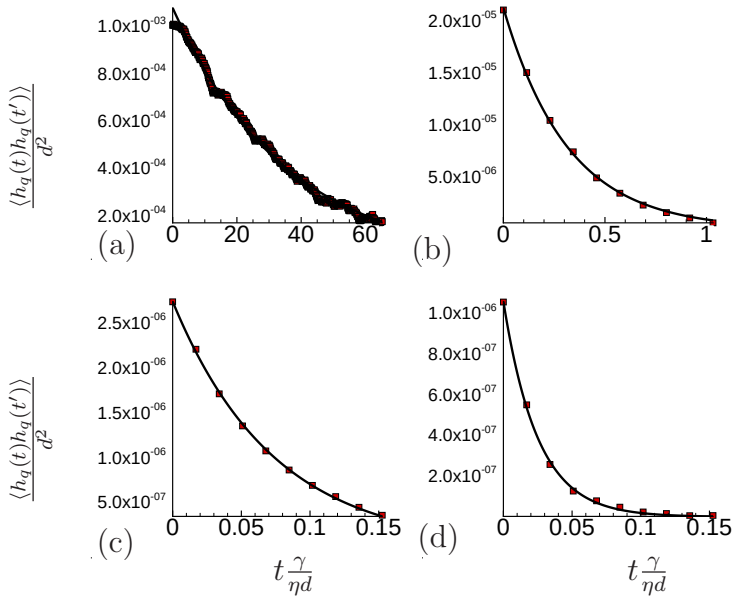

Figure 4.2: Example exponential fits $e^{-\omega t}$ of $\langle h_q(0)h_q(t)\rangle/d^2$ for the 12σ (4nm) simulation: (a) $q\sigma = .05$, (b) $q\sigma = .32$, (c) $q\sigma = .95$, and (d) $q\sigma = 1.66$.

tive of a molecular scale phenomenon, and thus insensitivity to the film thickness d. To better understand the relevant parameters for new $\omega \sim q^2$ regime, we simulated several other films. The first has an increased temperature, from $k_BT = 0.83\epsilon$ to $k_BT = \epsilon$. This obviously increases the energy of the perturbations, but also decreased both surface tension and viscosity. The decay rates of the thermal capillary waves as functions of q for both 6σ and 12σ are plotted in Figure 4.7, along with the data at the lower temperature. The increase in temperature and decrease in surface tension has the expected effect of increasing the mean squared amplitude of the perturbations by 1.8 as predicted by (2.35). As shown in Figure 4.7, the ω data are independent of temperature. This suggests that interface displacements are not the dominant length scale of the new $\omega \sim q^2$ dynamics and the linear assumption made in 2.2 seems valid.

Figure 4.8 shows that the $\omega \sim q^2$ region no longer collapses for the σ scaling when different polymers lengths are simulated. However, if the data are scaled by the ensemble average of the radius of gyration of the

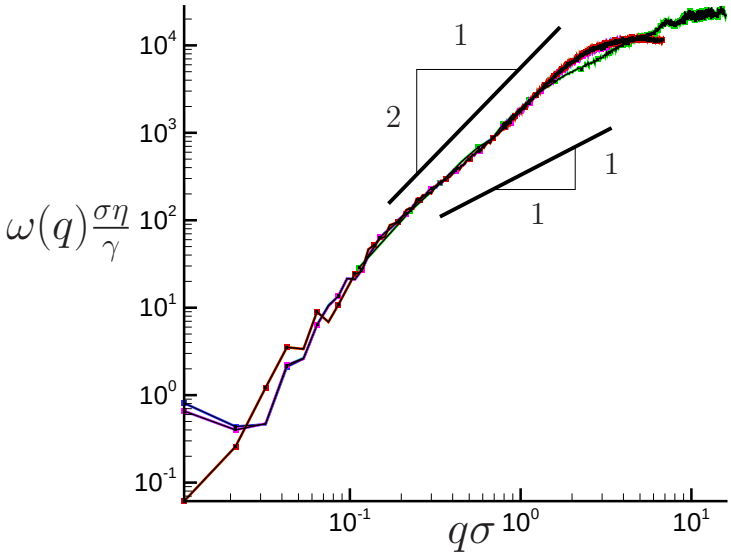

Figure 4.3: Overlaid curves showing the insensitivity of $\omega(q)$ to seven different sets of numerical averaging parameters for the 12σ (4nm) fluid film: $\tau_{\text{avg}} = \tau_{\text{LJ}}, V_{\text{bin}} = \sigma^3, \rho_c = \rho_{\text{bulk}}/10$; $\tau_{\text{avg}} = 2\tau_{\text{LJ}}, V_{\text{bin}} = \sigma^3, \rho_c = \rho_{\text{bulk}}/10$; $\tau_{\text{avg}} = \tau_{\text{LJ}}, V_{\text{bin}} = .5\sigma^3, \rho_c = \rho_{\text{bulk}}/10$; $\tau_{\text{avg}} = \tau_{\text{LJ}}, V_{\text{bin}} = .25\sigma^3, \rho_c = \rho_{\text{bulk}}/10$; $\tau_{\text{avg}} = \tau_{\text{LJ}}, V_{\text{bin}} = \sigma^3, \rho_c = \rho_{\text{bulk}}/6$; $\tau_{\text{avg}} = \tau_{\text{LJ}}, V_{\text{bin}} = \sigma^3, \rho_c = \rho_{\text{bulk}}/16$; and $\tau_{\text{avg}} = \tau_{\text{LJ}}, V_{\text{bin}} = .02\sigma^3, \rho_c = \rho_{\text{bulk}}/10$. Also included for reference are two solid lines of slopes one and two. The high resolution data ($V_{\text{bin}} = .02\sigma^3$) is plotted in green and as expected only deviates for wavelengths approaching the bin size of the $V_{\text{bin}} = \sigma^3$ data.

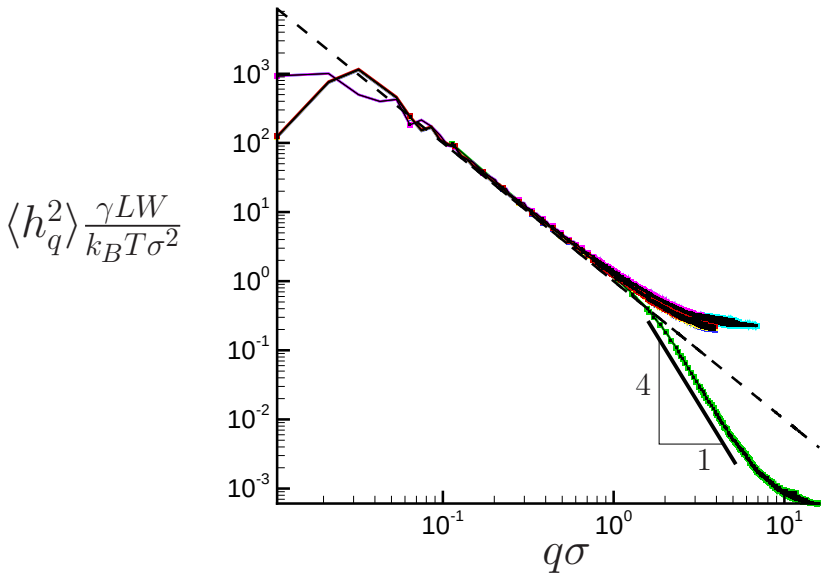

Figure 4.4: Overlaid curves showing the insensitivity of $\langle h_q^2 \rangle$ to seven different sets of numerical averaging parameters for the 12σ (4nm) fluid film: $\tau_{\text{avg}} = \tau_{\text{LJ}}, V_{\text{bin}} = \sigma^3, \rho_c = \rho_{\text{bulk}}/10$; $\tau_{\text{avg}} = 2\tau_{\text{LJ}}, V_{\text{bin}} = \sigma^3, \rho_c = \rho_{\text{bulk}}/10$; $\tau_{\text{avg}} = \tau_{\text{LJ}}, V_{\text{bin}} = .5\sigma^3, \rho_c = \rho_{\text{bulk}}/10$; $\tau_{\text{avg}} = \tau_{\text{LJ}}, V_{\text{bin}} = .25\sigma^3, \rho_c = \rho_{\text{bulk}}/10$; $\tau_{\text{avg}} = \tau_{\text{LJ}}, V_{\text{bin}} = \sigma^3, \rho_c = \rho_{\text{bulk}}/6$; $\tau_{\text{avg}} = \tau_{\text{LJ}}, V_{\text{bin}} = \sigma^3, \rho_c = \rho_{\text{bulk}}/16$; and $\tau_{\text{avg}} = \tau_{\text{LJ}}, V_{\text{bin}} = .02\sigma^3, \rho_c = \rho_{\text{bulk}}/10$. The high resolution data ($V_{\text{bin}} = .02\sigma^3$) is plotted in green. This higher resolution data shows additional high wavenumber agreement of measured amplitudes with (2.35). The dashed black line is (2.35) and the solid black line is for reference.

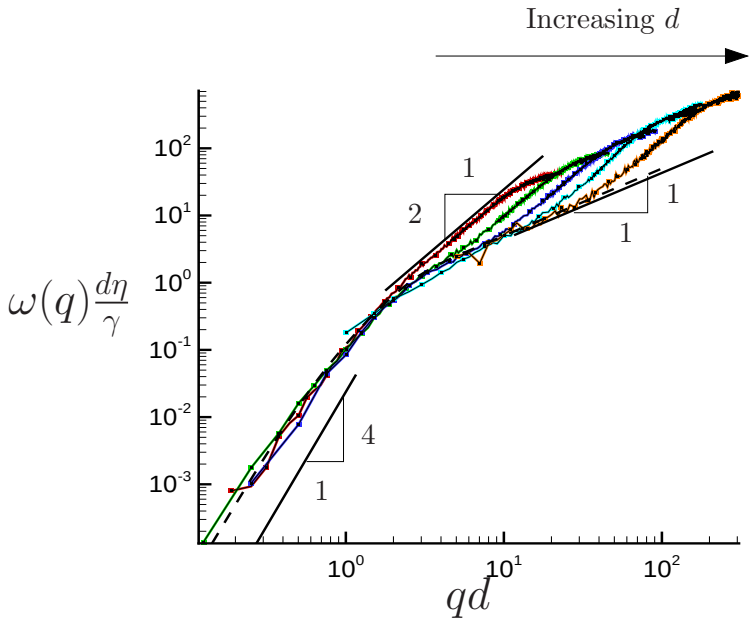

Figure 4.5: Calculated decay rates $\omega(q)$ as a function of wavenumber amplitude $q = |\mathbf{q}|$ for five films with different thicknesses: 6σ, 12σ, 24σ, 48σ, and 96σ. The black dashed line shows (2.51).

molecular chains

$$r_g \equiv \left\langle \sqrt{\frac{1}{N}\sum_{i=1}^{N}(\mathbf{r}_i - \mathbf{r}_{\text{mean}})^2} \right\rangle, \tag{4.3}$$

the $\omega \sim q^2$ region for the three polymer lengths collapse onto the same power law. In (4.3), N is the number of monomers per molecular chain, $\langle ... \rangle$ denotes an ensemble average, and $\mathbf{r}_i$ and $\mathbf{r}_{\text{mean}}$ are the position vector of atom i and average position of all atoms in the molecule, respectively. The quantity r_g was measured from bulk samples of each respective polymer. This dependence upon a length scale related to the molecular size of the fluids suggests a molecular-scale granularity effect.

4.3 Summary & Discussion

While it is not surprising that the atomistically simulated films show the continuum $\omega \sim q^4$ and $\omega \sim q$ behaviors, it is unexpected that there is a distinct, approximate $\omega \sim q^2$ behavior at short wavelengths. That this collapses to a single curve when scaled by the radius of gyration of the fluid

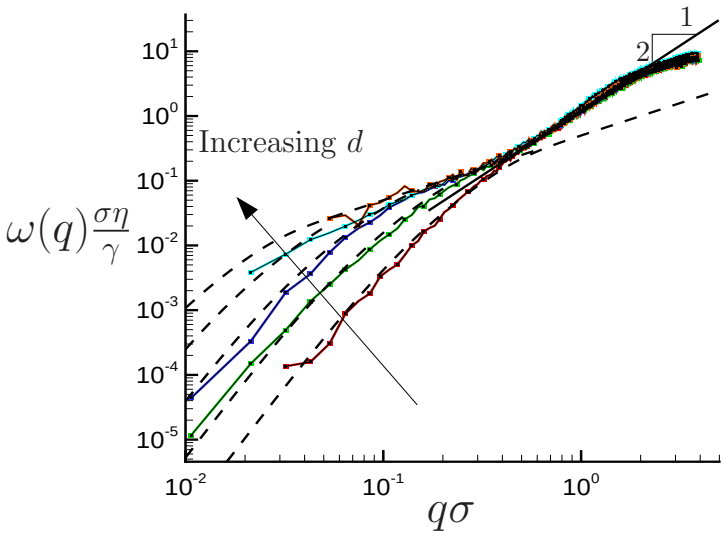

Figure 4.6: Same as Figure 4.5 but here scaled by the Lennard–Jones length scale σ.

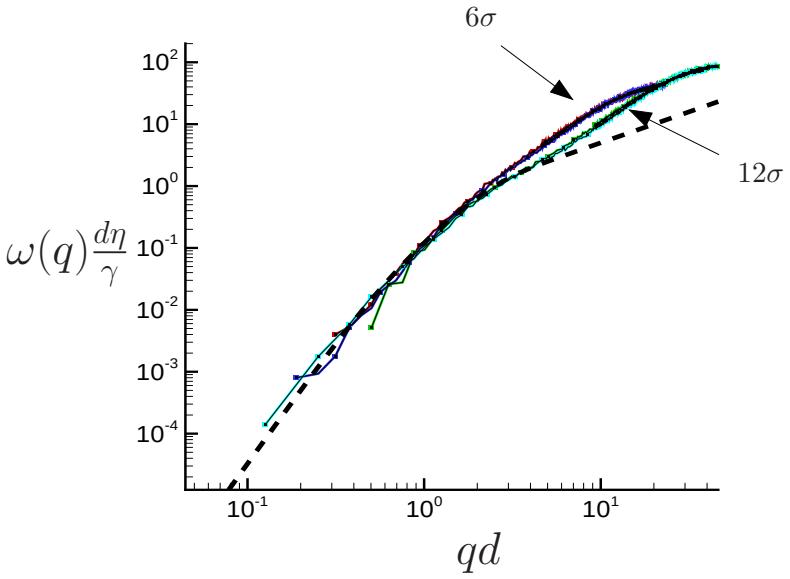

Figure 4.7: Decay rates of capillary waves for both the 6σ and 12σ films at temperatures $T = 0.82\varepsilon/k_B$ and $T = \varepsilon/k_B$. Data are indistinguishable except at small q, where statistical sample size effects are apparent for these simulations.

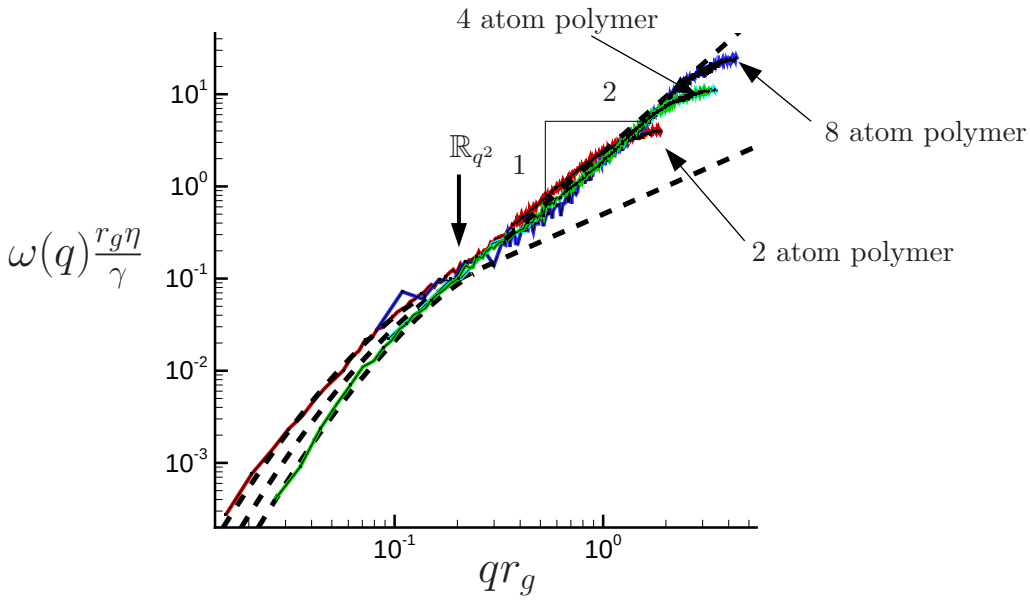

Figure 4.8: Relaxation rate for r_g scaled data. The 4-polymer data are plotted from two simulations with different domain shapes ($8\sigma \times 590\sigma$ and $50\sigma \times 50\sigma$), confirming that the is no artifact of the domain shape. The arrow labeled with $\mathbb{R}_{q^2}$ marks a nominal start of the $\omega \sim q^2$ regime.

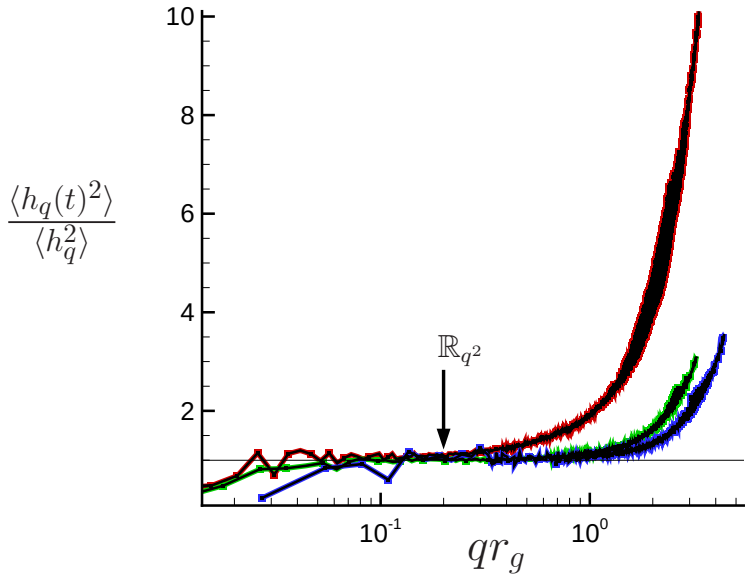

Figure 4.9: Ratio of the mean-squared amplitude $\langle h_q(t)^2\rangle$ to thermal capillary wave predictions (2.35) for the **2-polymer**, **4-polymer** and **8-polymer** as a function of qr_g. A black solid line is drawn at $\langle h_q(t)^2\rangle/\langle h_q^2\rangle = 1$, which represents the obvious predictions of (2.35). The arrow corresponds to that shown in Figure 4.8, marking a nominal beginning of the $\omega \sim q^2$ regime.

molecules suggests that dynamics in this new regime depends upon the wavelength of the perturbation relative to the average spatial extent of the fluid molecules, thus suggesting a granular effect, though its specific cause remains unclear.

The wavelength corresponding to the point marked by $\mathbb{R}_{q^2}$ in Figure 4.8 is 14σ. This is similar to the length scale at which atomistic fluids are seen to deviate from continuum predictions in confined channel flows, for example. Molecular simulations with simple fluids suggest that Newtonian fluid flow is usually achieved for channel flows with widths greater than 10σ,[62,63] which is comparable in size to the beginning of the $\omega \sim q^2$ regime.

Although we used a simple cutoff density to define our interface, as described in Section 4.1, there are some subtleties of a liquid-vapor interface at the molecular level that must be discussed. Tarazona and Chacón[59,60] report intrinsic density fluctuations at the interface of monoatomic Lennard–Jones fluids. These fluctuations are manifestations of molecular ordering near the surface of the fluid and cause obvious concerns for cutoff density based definitions, such as employed in this work. Tarazona and Chacón[59,60] emphasize that these fluctuations were particularly pronounced for atomic Lennard–Jones fluids well below the critical temperature T_c, and as film temperatures approaches T_c this molecular ordering near the interface becomes less pronounced and yields smoother intrinsic density profiles.

For the different polymer lengths simulated, our films effectively span a range of T/T_c values. With a $T/T_c \approx 0.70$,[64] the 2-atom polymer at $T = \epsilon/k_B$ shown in Figure 4.7 has the highest relative temperature, while the $T = 0.83\epsilon/k_B$ 8-polymer, which appeared to have no gas phase at this temperature, has a significantly lower T/T_c. Large T/T_c values, such as 0.70, are not expected to show any significant density fluctuations near the fluid-vapor interface.[60] If intrinsic fluctuations in the interface density were affecting the interface measurement, they are expected to be sensitive to T/T_c.[59,60] Since we see no such sensitivity, we conclude they are not a significant factor in this study.

The fluctuations in this new regime are fast, but not fast enough to introduce any obvious inertial effects. Consistent with the viscous con-

tinuum model (2.36), the decorrelation of the surface waves is indeed exponential as seen in the examples shown in Figure 4.2. The fluctuation Reynolds number is also low. For $U = \omega h_q$ and $L = 1/q$, $Re = \rho UL/\eta = 0.01$ near the switch from $\omega \sim q$ to $\omega \sim q^2$ behavior at around $q\sigma = 0.45$ (see Figure 4.8). From (2.35), the capillary amplitudes scale as $h_q \sim 1/q$, so the calculated Re should not deviate significantly from this value throughout the quadratic decay regime.

Interestingly, including a slip boundary condition on the wall yields a $\omega \sim q^2$ decay behavior in the long-wavelength limit,[22] but slip can only be significant when the relaxation of the capillary waves is directly affected by the wall, not for wavelengths shorter than those in the $\omega \sim q$ regime. Including slip lengths into the fluid model[22] shifts the lubrication, $\omega \sim q^4$, predictions decay rates toward smaller q in an $\omega(q)$ plot such as in Figure 4.5. Such a shift would push continuum predictions (black dashed line) away from the already well modeled lubrication regime of all of our films. Furthermore, by inspection the velocity of fluid atoms adjacent to the fluid-solid interface revealed no evidence of slip.

It could be suggested that this new behavior is a manifestation of a more visco-elastic nature of the fluid at very fast timescales. Larger size polymers, with radii of gyrations greater than half the film thickness ($d \leq 2r_g$), have shown behavior indicative of visco-elastic properties.[18,24] In a theoretical analysis of several different thin film models, Henle *et al.*[22] showed that a non-slipping, inelastic fluid's height-height correlations would have multiple exponential decay rates, as well as decay rates that are constant relative to wavenumber q. Neither of these features appear in our simulations. As shown in Figure 4.2 and Figure 4.8, the correlations were well fitted by a single exponential decay and measured decay rates showed no q-independent behavior.

It could also be suggested that a deviation in the behavior from the continuum model is related to a wavenumber dependent surface tension $\gamma(q)$. Because surface tension drives the perturbations of the interface back towards equilibrium, a change in the effective surface tension could effect the relaxation rates. At high enough wavenumbers, where wavelengths approach molecule size, molecular deformation as well as interface defor-

mations could store the potential energy of the thermal fluctuations. This consideration was originally included into interface studies by Helfrich[65] and is found to be consistent with both molecular simulations[60] and x-ray spectroscopy.[66] Including bending interactions of molecules into the surface energy of an interface yields an effective surface tension of the form[60,65,66]

$$\gamma(q) = \gamma_o + \kappa q^2 + O(q^4), \tag{4.4}$$

where κ is a molecular stiffness term to account for energy being stored in molecular bending and γ_o is the large-scale wavenumber independent surface tension. Density functional theory provides an additional consideration for the effective surface tension $\gamma(q)$ of a fluid-vapor interface.[67,68] Mecke *et al.*[67,68] included the non-local interactions of the fluid atoms which create a local minimum in $\gamma(q)$ at higher wavenumbers before molecular bending dominated the effective surface tension, $\gamma(q) \sim q^2$. However, as is apparent in Figure 4.9, the constant surface tension predicts $\langle h_q^2 \rangle$ well past the beginning of the the approximate $\omega \sim q^2$ behavior. Using higher resolution binning data (Figure 4.4), we were able to resolve an apparent transition to a molecular bending regime $\langle h_q^2 \rangle \sim 1/q^4$, which occurs at higher wavenumbers than $\mathbb{R}_{q^2}$. The higher resolution binning data did not resolve the predicted localized minimum of Mecke *et al.*, however our results are consistent with the results from the molecular simulations of Chacón and Tarazona[59,60] who also employed at 2.5σ cutoff radius in their Lennard–Jones fluid simulation. Given that the amplitudes of the thermal capillary waves were consistent with capillary wave theory for $qr_g > \mathbb{R}_{q^2}$ for both the lower resolution binning ($V_{\text{bin}} = \sigma^3$) as well as our higher resolution data ($V_{\text{bin}} = .02\sigma^3$), there is no reason to believe that wavenumber dependent surface tension explains the apparent $\omega \sim q^2$ regime.

It is noteworthy that the viscosity η and surface tension γ still seem relevant in the new regime. They vary by factors of 7.7 in η and 2 in γ, yet the data still collapse when scaled by these parameters in Figure 4.8. The onset of $\omega \sim q^2$ also does not seem to correspond to any obvious failure of the surface tension Laplace pressure model (2.30), as must occur at molecular scales. We assess this by gaging whether or not the surface energy implied by (2.30) obeys equipartition (2.35). Equipartition must be obeyed, of course, and it indeed is in the atomistic simulations; this test is an in-

direct assessment of whether or not (2.30) provides a reasonable model for the surface energy when $\omega \sim q^2$. In Figure 9, the $\mathbb{R}_{q^2}$ point, which labels the onset of $\omega \sim q^2$ behavior, does not correspond to a consistent deviation from equipartition for the standard surface tension model as defined by (2.30) and (2.35). The 2-polymer case does deviate here, but the longer polymers seem to follow (2.35) well into the $\omega \sim q^2$ regime. However, as shown in Figure 4.4, this apparent breakdown of surface tension in the 2-polymer fluid is an artifact of the bin sized use in the $\rho(x, y, z, t)$ calculation and is not present in the the higher resolution data.

Given all this, one possibility is that a failure of the applicability of the Newtonian stress tensor (2.46) at these molecular scales is responsible for the new behavior. The dynamics of thermal capillary waves are a balance of the power dissipated from relaxation of the surface perturbation against the Laplace pressure and the dissipated energy of the flow underneath the fluid surface. Our amplitude measurements suggest that the Laplace pressure measurements are accurate well into the new regime (Figure 4.9). Since the dissipation of energy against the Laplace pressure must be balanced against viscous dissipation in $Re \rightarrow 0$ flows, and our decay rates are faster than expected than under Newtonian dissipation (Figure 4.6), the dissipation of the flow near the interface must be less than the expected dissipation under Newtonian assumptions. However, given that there is a collapse of data relative to Newtonian shear viscosity, it is implied that there is a connection between the "new" shear stress and the Newtonian shear stress. Perhaps this connection can be derived from a granular flow treatment similar to that of Haff.[69] Another possibility is that the strain-rate tensor used in the development of (2.51) may need to be modified to account for the discrete size of the fluid elements. Thus, rather than assuming a continuous derivative across the velocity field, strain rate may be better modeled as a finite difference between layers of atoms with grid spacing roughly r_g.

It seems that further numerical, experimental, and theoretical investigations are needed to fully explain the observed larger q decay rate behavior. Given that this approximated $\omega \sim q^2$ regime is a function of particle size, it may become apparent at larger, more engineering relevant, length scales in fluids with larger molecules.

Chapter 5

The Enhanced Spreading of a Droplet Due to Thermal Fluctuations

This second main project presented in this dissertation has two main objectives. Firstly, it is designed to test whether thermal fluctuations can drive bulk fluid flow, as predicted by Davidovitch *et al.*,[9] and discussed in Section 2.4. Secondly, it will test whether the thermally augmented continuum model of thin film flow, derived in Section 2.3, accurately predict the expected, enhanced spreading of a spreading atomic droplet on a plate. To study this, we compared numerical solutions of the continuum model (see Section 3.4) against a molecular simulation of a spreading atomic drop (see Section 3.1).

5.1 Review of Methods

As discussed in Section 3.1.1, all atoms in the simulation are modeled with a Lennard–Jones pair potential, which includes a $1/r^6$ dispersion (van der Waals) attraction and an empirical $1/r^{12}$ repulsion. The simulations employ a cutoff radius $r_c = 2.5\sigma$, the implications of which are covered in Sections 3.2.3– 3.2.4. Specifically, the surface tension is decreased by a factor of almost 2,[46] while disjoining pressure vanishes for films thicker than r_c. Although disregarding disjoining pressures limits the possible real fluid situations where these thermal fluctuations matter, according to the scaling analysis of Davidovitch,[9] for normal values of disjoining pressures, one would expect to still see thermal forcing dominate in one-dimensional spreading drops or one-dimensional fluid 'creeping' problems. Two-dimensional droplets of real liquids are unlikely to enter a thermal dominated spreading because of the narrow range in which thermal forces would dominate both surface tension and disjoining pressure.

To suppress evaporation and condensation, which would muddle results, Lennard–Jones atoms are joined into polymers using the Finite Extensible Nonlinear Elastic (FENE) potential,[36,58] as discussed in Section 3.1.2.

The atomistic simulation contained 68134 fluid atoms and 44200 wall atoms. The fluid atoms were in two-atom 'polymers'. Each atom had a mass of $m_f = m$. The interaction energy between all fluid and solid atoms was the same: $\varepsilon_{ff} = \varepsilon_{sf} = \varepsilon$. The values of the molecular parameters were set to match that of liquid argon as listed in Table 3.1. As shown in Figure 5.1, the solid atoms were arranged into 4 layers of an FCC lattice of length 1760σ in x and depth (into the page) of 8σ in z. The melting temperature of the solid atoms was decreased by taking $m_s = 10m$ and $\varepsilon_{ss} = 10\varepsilon$.

Time integration was carried out via the velocity Verlet algorithm (see Section 3.2.1), which has excellent but not exact conservation properties. Because of the long times of these simulation, weak thermostats were applied to maintain the temperature, as described in Section 3.2.2. The substrate upon which the fluid was attached maintained its temperature through an Andersen[38] thermostat while the bulk of the fluid drop had a weak Bersenden[37] thermostat applied. The strength of the Bersenden thermostat was set at a value weaker than what has been shown to reproduce the power spectra of potential energy fluctuations and diffusivity of simulated water molecules when compared to a system with no thermostat applied.[42]

The initial condition was generated by 'cutting' out a droplet shape from a flat thermally equilibrated thick fluid film. A precursor film was also included over the whole domain (see Figure 5.1), whose thickness was set to be slightly larger than the cutoff radius of the potential (3.1). This choice simplifies analysis by essentially removing any disjoining pressure effects. Because our cutting procedure introduces a non-equilibrated shape to our drop from an equilibrated flat profile, there is an initial period of local equilibration where a large amount of evaporation takes place. As shown in Figure 3.3, a portion of the simulation was not included in results and our 'time zero', from which the initial conditions for (2.87) were

defined, was the end of this initial period of equilibration seemed to have ceased. Different choices for this 'time zero' do not alter the conclusions of this work.

Equation (2.87), the model of an evaporating stochastic lubrication equation, was solved with an implicit Crank-Nichcolson-like time integration and a Fourier collocation discretization in x, the details of which are described in Sections 3.4.1 and 3.4.2. The initial condition was taken as the measured interface of the molecular spreading drop as defined by the density isopleth $\rho_c = \rho_f/10$, where ρ_f is the bulk fluid density. Results are insensitive to our choice of ρ_c. Ten such stochastic solutions are averaged to produce ensemble averaged spreading solutions.

For direct comparison between the molecular simulation and the predictions of the continuum model (2.87), the physical parameters of the molecular fluid needed to be independently determined (see Table 5.1). Using small samples of the molecular fluid, thermal conductivity k, viscosity η, and surface tension γ were all calculated using the established techniques[39,70] discussed in Sections 3.3.1 and 3.3.2. The latent heat of vaporization $\mathcal{L}$, which is important for modeling evaporation, was less straightforward to estimate and required novel techniques that are described in Section 3.3.3. Though there is clearly finite evaporation and condensation, which motivated its inclusion in the model, it should also be clear evaporation played a relatively small role in the dynamics. The drop spread primarily by other mechanisms.

Symbol	Description	Value
T	equilibrium temperature	100 K
ρ	fluid density	1365 kg/m^3
ρ_v	vapor density	33.6 kg/m^3
$\mathcal{L}$	latent heat of vaporization	649 kJ/kg
k	thermal conductivity	0.0991 J/m
η	viscosity	1.101×10^{-4} kg/ms
γ	surface tension	1.07×10^{-2} kg m^2/s^2

Table 5.1: Properties of the molecular fluid.

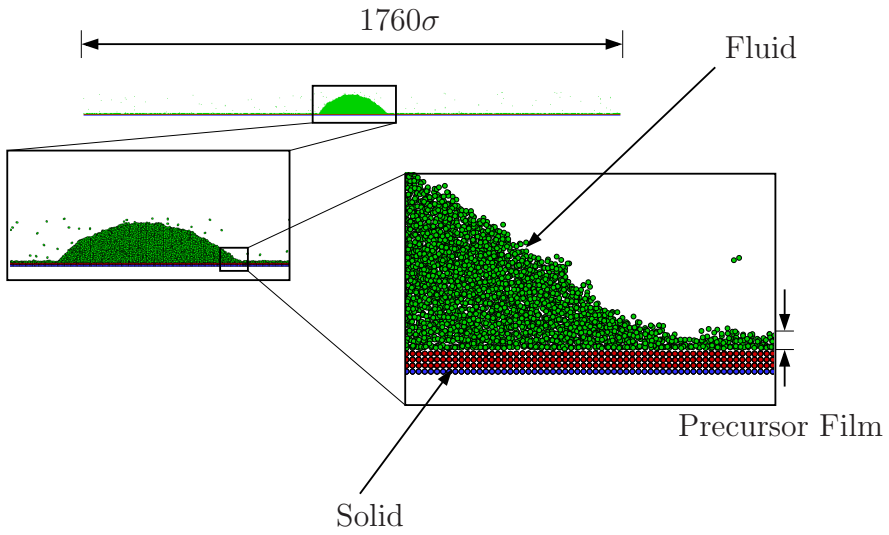

Figure 5.1: Simulation domain chosen to obey Davidovitch *et al.* inequalities (2.100) are satisfied.

5.2 Results

A large molecular simulation was used to directly compare the predictions of the stochastically augmented evaporating lubrication equation (2.87). (The domain of the simulation is shown in Figure 5.1). This particular domain is chosen with a precursor film with thickness greater the truncation length of the Lennard-Jones potential r_c, thus disjoining pressure does not effect dynamics. In order to avoid granularity effects and focus on the fluid dynamics of molecular flows, the size of the drop is chosen such that the drop had a large enough initial height, $h_o = 50\sigma$, to allow significant spreading to occur before becoming only several atoms thick. Significant spreading is necessary to observe thermally driven dynamics because it allows curvature in the fluid-vapor interface to decrease such that capillary forces could be dominated. Furthermore, the length of the domain (1760σ) was chosen to avoid any interaction in the spreading between the periodic images of the drop. All of these considerations numerically obeyed the equalities of Davidovitch *et al.*,[9] (2.100) which were shown to allow thermally dominated spreading.

In order to verify the quality of the approximated latent heat of vaporization, the average film thickness, far away from the spreading droplet, was measured as a function of time, shown in Figure 5.2. The average film

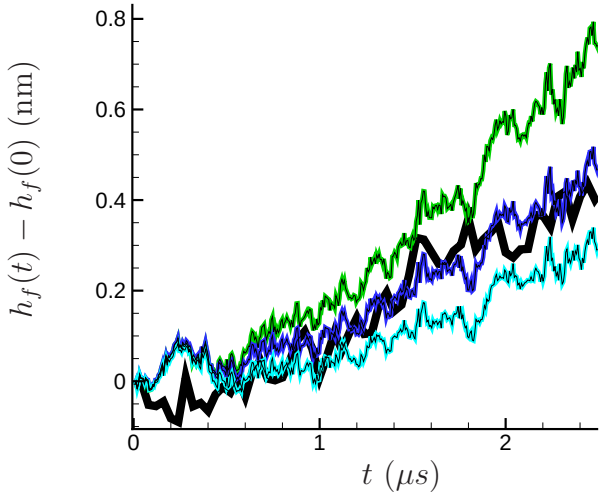

Figure 5.2: Precursor film thickness in **black** compared with predictions of (2.87) for different latent heats: $\mathcal{L}/2$, $\mathcal{L}$, and $3\mathcal{L}/2$.

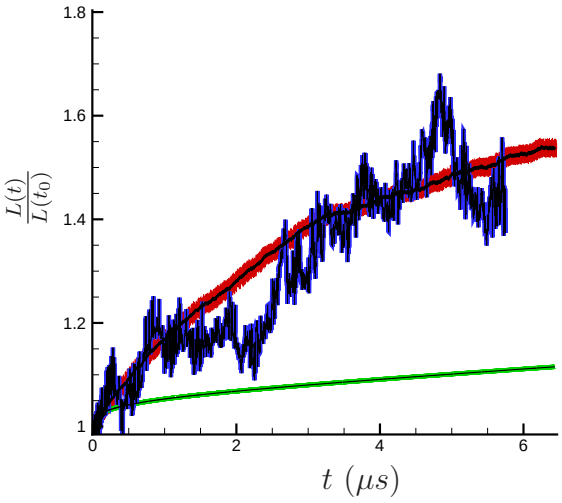

Figure 5.3: Drop spreading: molecular simulation, stochastic lubrication model (ensemble average of ten simulations), and the standard lubrication model.

thickness $h_f(t)$, in both the molecular and numerical simulation was averaged over a distance of $L_b/8$ on at each edge such that

$$h_f(t) = 4/L_b \left[\int_0^{L_b/8} h(x,t)\mathrm{d}x + \int_{7L_b/8}^{L_b} h(x,t)\mathrm{d}x \right], \tag{5.1}$$

and L_b is the domain length. Because of the large distance of the regime where $h_f(t)$ is measured to the placement of the drop, the accumulation of fluid at these boundaries can only be attributed to evaporation and condensation. The almost identical accumulation of fluid at the edge of both the molecular simulation as well as the numerical solution of (2.87) is a reflection of the quality of the evaporation parameter $\mathcal{L}$ used to construct the evaporation parameter δ_v (2.68) in our continuum model. As shown, our choice of latent heat of vaporization $\mathcal{L}$ models the condensation well when compared to $\mathcal{L}/2$ and $3\mathcal{L}/2$. This validates our method for determining of latent heat of vaporization described in Section 3.3.3.

To quantify the spreading of the drop, we define its width L via the second moment about its center x_c:

$$L^2(t) = \frac{\int_0^{L_b} h(x,t)(x-x_c)^2 \, \mathrm{d}x}{\int_0^{L_b} h(x,t) \, \mathrm{d}x}. \tag{5.2}$$

Figure 5.3 compares $L(t)$ for the atomistic simulation, the average of 10 realizations of the stochastically augmented lubrication equation, and the standard lubrication equation. Clearly, there is a poor comparison with the standard lubrication model, whereas the averaged solution of the stochastic lubrication model appears to follow the atomistic simulation results.

5.3 Summary and Discussion

Though this comparison is striking, it should be clear that this relative importance of the stochastic spreading term is not expected in all cases. Davidovitch *et al.*[9] discusses why this type of thermal spreading would only be found in certain regimes. For self-similar spreading drops with initial height h_o, they showed that thermal forcing should dominate the sur-

face tension only when

$$h(t) \ll \frac{h_o^2}{x^*} \qquad \text{and} \qquad |x - x_c| \gg x^*, \tag{5.3}$$

with $x^* = h_o^{7/6} W^{1/6} / l_T^{1/3}$ and h_t the current height of the drop. What (5.3) indicates is that drop needs to be relatively flat, so that the pressure supplied from the curvature in the interface is relatively small, and that stochastic stress dominated spreading will occur in regions farther away from the drop center than x^*. The first inequality is the more difficult to satisfy in atomistic simulations, because it requires relatively long run times, while the second inequality is often obtained in any large molecular simulation of spreading drops.[30,58] Clearly, the smallness of W in our case makes both these conditions easier to satisfy. Our simulation ran for almost $3 \times 10^6 \sqrt{m\sigma^2/\varepsilon}$ time units, but it still only slightly surpassed the first condition as a simple inequality, $h = 5.6$nm being only slightly less than $h_o^2/x^* = 6.4$nm. Other simulations of shorter spreading times or of higher viscosity drops would not spread far enough to enter into this regime. Another challenge is achieving enough spreading for it to be noticeable, which motivated our choice of fluid. The two-atom-polymer model was selected as a balance between having a low enough viscosity that enough spreading could occur but small enough evaporation that spreading is still the dominant mode of fluid transport.

This matching of the stochastic lubrication model with the molecular fluid behavior suggests that the assumptions used in developing the stochastic-evaporating lubrication equation (2.87) are appropriate for molecular fluids in regimes where dynamics are dominated by thermal fluctuations. Also, the drastic difference in the predictions between the stochastic and non-stochastic fluid model demonstrate the importance of considering thermal fluctuations at length scales approaching l_t.

Chapter 6

Conclusions

The goal of this dissertation was to investigate the dynamics of thin liquid films at length scales where thermal fluctuations were expected to affect mechanics. These fluctuations, from the thermal energy of the fluid molecules, perturb fluid interfaces. However, for many fluids, the length-scale of these perturbations is near the size of the fluid molecules. This suggests the question of whether continuum modeling contains the essential physics necessary to predict the behavior of these thermally perturbed fluid films.

Thus the first project of this dissertation focused upon studying the dynamics of simulated molecular fluid flows and compared this behavior directly to predictions of continuum models. More particularly, in order to first test whether continuum modeling is applicable to thermally perturbed films, we investigated the relaxation rates of thermal capillary waves (see Chapter 4). Thermal capillary waves are the small amplitude fluctuations in a stable fluid film interface due to the thermal energy of the fluid, that then relax due to the surface tension driving the interface back to the equilibrium configuration against the resistance of fluid viscosity. According to equipartition, each degree of freedom should have $k_B T/2$ of energy and within the continuum model the amplitudes of these perturbations are small. Thus we can linearize the dynamics of the continuum interface and study the decay rate of each of the Fourier modes of the interface perturbations independently. The continuum solution of the different Fourier modes was then compared with the Fourier modes of the fluid-vapor interface from molecular dynamics simulations. These comparisons demonstrated two things: for all wavelengths greater than 20 radii of gyration of the fluid molecule, continuum predictions matched well with the molecular behavior for almost a decade of length scales and over 3 decades of relaxation times,

and for wavelengths less than about 20 radii of gyration, an unexpected behavior was found. In this regime of unexpected behavior, the decay rates of the perturbations were still related to bulk values of viscosity and surface tension. However, the decay rates also scaled by a new lengthscale, namely the radii of gyration of the fluid molecules for 2-, 4-, and 8-atom polymer fluids. Further analysis of this new regime suggested that the breakdown in the continuum modeling is due to the Newtonian stress tensor overestimating the dissipation of the molecular fluid flow. Although no definitive physical explanation could be provided, this overestimation is expected to be an artifact due to the fact that a continuous derivative of fluid velocity is used in the Newtonian stress tensor to approximate what is essentially a finite difference between layers of fluid atoms with grid spacing roughly equal to the molecular radius of gyration.

This breakdown of continuum mechanics leaves open an opportunity for future research into the mechanism of this hybrid regime, where flow dynamics are a function of both continuum and granular properties of the fluid. This hybrid-flow flow regime may be necessary in future applications when designing nanometer length devices. It could also manifest itself at larger length scales when larger size polymers are being used in the manufacturing of small-scale technologies. Future studies could include computational investigations to map out the behavior of a larger range of fluids with increased radii of gyrations, as well as collaboration with experimental investigations of liquid polystyrene films or colloid-polymer interfaces to identify this new regime in real fluids.

However, the overall success of modeling all but the smallest length scales in thermally perturbed thin liquid films motivates further studies. Because it focused upon the linearized dynamics of equilibrium fluid interfaces, the capillary waves study of Chapter 4 is representative of only a small subset of thin film phenomena. The next logical step was an investigation of a non-equilibrium fluid phenomenon whose dynamics are predicted to be dominated by thermal fluctuations. The scaling analysis of Davidovitch *et al.*[9] suggested that thermal fluctuations can dominate thin film spreading dynamics. Verification of such a prediction would have several benefits. The first benefit being, phenomenologically it would be of value to verify that thermal fluctuations can dominate molecular fluid

behavior, not just perturb interfaces. A second benefit would be, by expanding the evaluation of continuum models to more realistic nanometer scale fluid flows, we can further investigate the essential physics needed in modeling future nanoscale devices.

The second project of this dissertation (see Chapter 5) studies the spreading of a simulated molecular fluid drop upon a wetting crystal interface. In the abscence of thermal fluctuations, the spreading of droplets at nanometer scales is primarily driven by surface tension and its balance against viscous forces. However, at nanometer scales, droplet spreading is hypothesized to increase via fluctuation mechanisms[9] due to thermal stresses dominating surface tension stresses. The molecular spreading drop we simulated had non-negligible evaporation, and thus our continuum model of this spreading drop needed to include both stochastic forcing and an evaporation model. Our simulations demonstrated that the spreading rate of a molecular drop closely matched the predictions of a thermally augemented continuumd model, whereas the non-thermal continuum model drastically underestimated the width of the drop as a function of time.

The success of the continuum modeling of a thermally spreading and evaporating droplet on a plate suggests several key points. Firstly, thermal fluctuations can affect bulk fluid flow in certain regimes where thermal stress can dominate over capillary forces. Although not all nanometer-scale flows require thermal considerations,[11,31] some as we have shown, do. Future analysis of thin film flow should at least consider contributions of thermal fluctuations. Secondly, continuum modeling has remarkable success in reproducing the behavior of molecular flows. This is supported not only by the success of the two studies of this dissertation, but other direct comparison to molecular flow.[11,30,31,58] The combination of our findings from both studies of this dissertation supports further investigations into the dynamics of thermally driven thin liquid films. For example, Grun *et al.*[10] demonstrated, by the numerical solutions of a stochastic lubrication equation, that the rupture time of unstable thin liquid films is decreased by almost an order of magnitude when thermal fluctuations were included into the continuum model. In addition to their obvious theoretical interest,[26,71–73] unstable thin films studies also have potential use in the creation of patterned[4] films. The study of such a phenomenon would be ideal

for molecular simulations and analysis with continuum models. These unstable films are seeded by thermal fluctuations, yet the work of Chapter 4 suggests that continuum modeling may not be adequate to predict molecularly thin film rupture. It is unclear if there would be any alteration in behavior when length scales of unstable thin films are less than 20 molecular radii of gyration. Perhaps at such scales, the Newtonian stress tensor's overestimation of viscous stress may reduce molecular rupture times from that of continuum predictions as well as affect the dominant length scale of rupture.

References

[1] J. Mendelson, S. Yang, J. Hiller, A. Hochbaum, and M. Rubner. Rational design of cytophilic and cytophobic polyelectrolyte multilayer thin films. Biomacromolecules, 4:96–106, 2003.

[2] E. Ostuni, C. Chen, D. Ingber, and G. Whitesides. Selective depositions of protiens and cells in arrays of microwells. Langmuir, 17:2828–2834, 2001.

[3] L. L. Lee, C. D. Schaper, and W. K. Ho. Real-time predictive control of photoresist film thickness uniformity. IEEE Transactions on Semiconductor Manufacturing, 15(1):51–59, 2002.

[4] E. Bormashenko, R. Pogreb, O. Stanevsky, Y. Bormashenko, T. Stein, Y. Z. Gaisin, R. Cohen, and O. V. Gendelman. Mesoscopic pattering in thin polymer films formed under the fast dip-coating process. Macromolecular Material Engineering., 290:114–121, 2005.

[5] M. Moseler and U. Landman. Formation, stability, and breakup of nanojets. Science, 289(5482):1165–1169, 2000.

[6] J. Eggers. Dynamics of liquid nanojets. Physical Review Letters, 89(8):084502, 2002.

[7] D. G. Aarts, M. Schmidt, and H. N. W. Lekkerkerker. Direct visual observation of thermal capillary waves. Science, 304:847–850, 2004.

[8] Y. Hennequin, D. G. A. L. Aarts, J. H. van der Wiel, G. Wegdam, J. Eggers, H. N. W. Lekkerkerker, and D. Bonn. Drop formation by thermal fluctuations at an ultralow surface tension. Physical Review Letters, 97(244502):244502, 2006.

[9] B. Davidovitch, E. Moro, and H. Stone. Spreading of viscous fluid drops on a solid substrate assisted by thermal fluctuations. Physical Review Letters, 95(244505):244505, 2005.

[10] G. Grun, K. Mecke, and M. Rauscher. Thin-film flow influenced by thermal noise. Journal of Statistical Physics, 122(6):1261–1291, 2006.

[11] J. B. Freund. Atomic detail of an evaporating meniscus. Physics of Fluids, 17(022104):022104, 2005.

[12] M. P. Allen and D. J. Tildesley. Computer Simulations of Liquids. Oxford Science Publications, Oxford, 1989.

[13] E. M. Lifshitz and L. D. Landau. Fluid Mechanics. Butterworth-Heinemann, Oxford, 2nd edition, 1987.

[14] A. Rahman. Liquid structure and self-diffusion. The Journal of Chemical Physics, 45(7):2585, 1966.

[15] B. Oksendal. Stochastic Differential Equations: An Introduction with Applications. Springer, New York, 6th edition, 2003.

[16] D. S. Lemons. An Introduction to Stochastic Processes in Physics. Johns Hopkins University Press, Baltimore, 2002.

[17] H. Kim, Z. Jiang, H. Lee, Y. J. Lee, X. Jiao, C. Li, L. Lurio, M. Rafailovich, and S. K. Sinha. Hydrodynamic surface fluctuations of polymer films by coherent x-ray scattering. Thin Solid Films, 515:5536–5540, 2007.

[18] Z. Jiang, H. Kim, X. Jiao, H. Lee Y. J. Lee, Y. Byun, S. Song, D. Eom, C. Li, M. H. Rafailovich, L. B. Lurio, and S. K. Sinha. Evidence for viscoelastic effects in surface capillary waves of molten polymer films. Physical Review Letters, 98:227801, 2007.

[19] Z. Jiang, H. Kim, S. G. J. Mochrie, L. B. Lurio, and S. K. Sinha. Surface and interfacial dynamics of polymeric bilayer films. Physical Review E, 74:011603, 2006.

[20] S. W. Sides, G. S. Grest, and M. D. Lacasse. Capillary waves at liquid-vapor interfaces: A molecular dynamics simulation. Physical Review E, 60(6):1–6, 1999.

[21] B. M. Ocko, X. Z. Wu, E. B. Sirota, S. K. Sinha, and M. Deutsch. X-ray reflectivity study of thermal capillary waves on liquid surface. Physical Review Letters, 72(2):242–245, 1994.

[22] M. L. Henle and A. J. Levine. Capillary wave dynamics on supported viscoelastic films: Single and double layers. Physical Review E, 75(021604):021604, 2007.

[23] R. L. C. Vink, J. Horbach, and K. Binder. Capillary waves in a colloid-polymer interface. The Journal of Chemical Physics, 122:134905, 2005.

[24] Y. S. Seo, T. Koga, J. Sokolov, M. H. Rafailovich, M. Tolan, and S. Sinha. Deviations from liquid-like behavior in molten polymer films at interfaces. Physical Review Letters, 94:157802, 2005.

[25] W. E. Wallace, D. A. Fisher, K. Efimenko, W. Wu, and J. Genzer. Polymer chain relaxation: Surface outpaces bulk. Macromolecules, 34:5081–5082, 2001.

[26] R. Fetzer, M. Rasuscher, R Seeman, K. Jacobs, and K. Mecke. Thermal noise influences fluid flow in thin films during spinodal dewetting. Physical Review Letters, 99:114503, 2007.

[27] A. Oron, S. Davis, and S. G. Bankoff. Long-scale evolution of thin liquid films. Reviews of Modern Physics, 69(3):931–979, 1997.

[28] H. E. Hupert. Flow and instability of viscous current down a slope. Nature, 300:427–429, 1982.

[29] V. Ajaev, G. M. Homsy, and S. J. S. Morris. Dynamic response of geometrically constrained vapor bubbles. Journal of Colloid and Interface Science, 254:346–354, 2002.

[30] D. R. Heine, G. S. Grest, and E. B. Webb. Surface wetting of liquid nanodroplets: Droplet-size effects. Physical Review Letters, 95:107081, 2005.

[31] G. He and N. G. Hadjiconstantinou. A molecular view of Tanner's law: molecular dynamics simulations of droplet spreading. Journal of Fluid Mechanics, 497:123–132, 2003.

[32] A. M. S.Tremblay, M. Aria, and E. D. Siggia. Fluctuations about simple nonequilibrium steady states. Physical Review A, 23(3):1451 – 1479, 1981.

[33] R. W. Schrage. A Theoretical Study of Interface Mass Transfer. Columbia University Press, New York, 1953.

[34] L. H. Tanner. Spreading of silicon oil drops on horizontal surfaces. Journal of Physics D, 12:1473–1485, 1979.

[35] B. Z. Dlugogorski, M. Grmela, and P. J. Carreau. Viscometric functions for FENE and generalized Lennard-Jones dumbell liquids in Couette flow. Journal of Non-Newtonian Fluid Mechanics, 48:303–335, 1993.

[36] M. Kroger, W. Loose, and S. Hess. Rheology and structural changes of polymer melts via non-equilibrium molecular dynamics. Journal of Rheology, 37(6):1057–1079, 1993.

[37] H. J. C. Berendsen, J. P. M. Postma, W. F. van Gunsteren, A. DiNola, and J. R. Haak. Molecular dynamics with coupling to an external bath. Journal of Chemical Physics, 81:3684–3690, 1984.

[38] H. Andersen. Molecular dynamics at constant pressure and/or temperature. Journal of Chemical Physics, 72:2384–2393, 1980.

[39] D. C. Rapaport. The Art of Molecular Dynamics Simulation. Cambridge University Press, 1997.

[40] D. Donnelly and E. Rogers. Symplectic integrators: An introduction. American Journal of Physics, 73:938–945, 2005.

[41] T. Schlick. Molecular Modeling and Simulation. Springer, New York, 2002.

[42] A. Mudi and C. Chakravarty. Effect of the Berendsen thermostat on the dynamical properties of water. Molecular Physics, 102(7):681–685, 2004.

[43] S. Plimpton. Fast parallel algorithms for short-range molecular dynamics. Journal of Computational Physics, 117:1–19, 1995.

[44] M. Deserno and C. Holm. How to mesh up Ewald sums I. A theoretical and numerical comparison of various particle mesh routines. J. Chemical Physics, 109(18):7678–7701, 1998.

[45] D. Frenkel and B. Smit. Understanding Molecular Simulations. Academic, New York, 1996.

[46] A. Trokhymchuk and J. Alejandre. Computer simulations of liquid/vapor interface in Lennard-Jones fluids: Some questions and answers. Journal of Chemical Physics, 111(18):8510–8523, 1999.

[47] A. Sharma. Many paths to dewetting of thin films: Anatomy and physiology of surface instability. European Physics Journal E, 12:397–408, 2003.

[48] J. Israelachvili. Intermolecular and Surface Forces. Academic Press, 1992.

[49] D. S. Viswanath and N. R. Kuloor. Heat of vaporization, surface tension, and temperature. The Journal of Chemical and Engineering Data, 11(1):69–72, 1966.

[50] M. S. Green. Markoff random processes and the statistical mechanics of time-dependent phenomena. II. Irreversible processes in fluids. Journal of Chemical Physics, 22:398, 1954.

[51] R. Kubo, M. Yokota, and S. Nakajima. Statistical-mechanical theory of irreversible processes. II. Response to thermal disturbances. Journal of the Physical Society of Japan, 12:1203–1211, 1957.

[52] R. Zwanzig and R. D. Mountain. High-frequency elastic moduli of simple fluids. Journal of Chemical Physics, 43:4464, 1965.

[53] J. H. Irving and J. G. Kirkwood. The statistical mechanical theory of transport processes: IV. The equation of hydrodynamics. Journal of Chemical Physics, 18:817–829, 1950.

[54] D. J. Evans and G. P. Morriss. Nonequilibrium Liquids. Academic Press, London, 1st edition, 1990.

[55] M. J. P. Nijmeijer, A. F. Baker, C. Bruin, and J. H. Sikkenk. A molecular-dynamics simulation of the Lennard-Jones liquid vapor interface. Journal of Chemical Physics, 89(6):3789–3792, 1988.

[56] P. Moin. Fundamentals of Engineering Numerical Analysis. Cambridge University Press, Cambridge, 1st edition, 2001.

[57] A. M. Willis and J. B. Freund. Thermal capillary waves relaxing on atomically thin liquid films. Physics of Fluids, 22(2):022002, 2010.

[58] D. R. Heine, G. S. Grest, and E. B. Webb. Surface wetting of liquid nanodroplets: Droplet-size effects. Physical Review E, 68:061603, 2003.

[59] E. Chacón and P. Tarazona. Intrinsic profiles beyond the capillary wave theory: A Monte Carlo study. Physical Review Letters, 91(16):166103, 2003.

[60] P. Tarazona and E. Chacón. Monte Carlo intrinsic surfaces and density profiles for liquid surfaces. Physical Review B, 70:235407, 2004.

[61] M. J. Regan, P. S. Pershan, O. M. Magnussen, B. M. Ocko, M. Deutsch, and L. E. Berman. Capillary-wave roughening of surface-induced layering liquid gallium. Physical Review B, 54:9730–9733, 1996.

[62] J. J. Magda, M. Tirrell, and H. T. Davis. Molecular dynamics of narrow, liquid-filled pores. Journal of Chemical Physics, 83:1888–1901, 1985.

[63] J. Koplik and J. R. Banavar. Continuum deductions from molecular hydrodynamics. Annual Review of Fluid Mechanics, 27:257–292, 1995.

[64] A. M. Willis and J. B. Freund. Enhanced droplet spreading due to thermal fluctuations. Journal of Physics: Condensed Matter, 21:464128, 2009.

[65] W. Helfrich. Elastic properties of lipid bilayers: Theory and possible experiments. Z. Naturf, 28:693–703, 1973.

[66] J. Daillant and M. Alba. High-resolution x-ray scattering measurements: I. Surfaces. Reports on the Progress of Physics, 63:1725–1777, 2000.

[67] C. Fradin, A. Braslau, D. Smilgies, M. Alba, N. Boudent, K. Mecke, and J. Daillant. Reduction in the surface energy of liquid interfaces at short length scales. Nature, 403:871–874, 2000.

[68] K. Mecke and M. Rauscher. On thermal fluctuations in thin film flow. Journal of Physics: Condensed Matter, 17:S3515–S3522, 2005.

[69] P. K. Haff. Grain flow as a fluid-mechanical phenomena. Journal of Fluid Mechanics, 134:401–430, 1983.

[70] D. Frenkel and B. Smit. Understanding Molecular Simulation. Academic Press, San Diego, 1996.

[71] R. Verma and A. Sharma. Defect sensitivity in instability of dewetting in thin liquid films: Two regimes of spinodal dewetting. Ind. Eng. Chem. Res., 46(10):3108–3118, 2007.

[72] Y. J. Wang and O. Tsui. Mean-field description of spinodal growth of surface waves on rupturing films. Journal of Non-Crystalline Solids, 352:4977–4982, 2006.

[73] Y. J. Wang and O. .K. Tsui. Unconventional spinodal surface fluctuations on polymer films. Langmuir, 22:1959–1963, 2006.